AN ABSTRACT OF THE THESIS OF

Matthew Robert Rueben for the degree of Honors Baccalaureate of Science in Mechanical Engineering presented on May 15, 2013. Title: Describing Tsunami Inundation and Debris Motion using Optical Measurement Methods in a Large-Scale Wave Basin.

Abstract Approved: _____

Daniel Cox

This thesis consists of two papers in manuscript format.  The first paper presents optical measurements of tsunami inundation through an urban waterfront in a laboratory wave basin.  The physical model was constructed at 1:50 scale and was an idealization of the town of Seaside, Oregon. The paper presents an analysis of the optical measurements made with two overhead video cameras, focusing on tracking the leading edge of the tsunami inundation through the urban waterfront.  The results show that the methodology provides high-resolution information in both time and space of the leading edge position, and that these data can be used to quantify the influence of large macro-roughness features on the tsunami inundation processes in laboratory settings.  The second paper presents optical measurements of debris movement and tsunami inundation through an unobstructed beach in a laboratory wave basin. The debris consisted of rectangular boxes and was placed unconstrained on a raised flat section of basin floor with no still water on the raised section. Debris movement was measured using two overhead video cameras and a novel object tracking algorithm. The results demonstrate the ability of the video data analysis to quickly and reliably measure the locations and orientations of multiple debris specimens.

Key Words: Tsunami, laboratory experiments, optical measurements, overland flow, debris

Corresponding e-mail address:  matthew.rueben@gmail.com

Describing Tsunami Inundation and Debris Motion using

Optical Measurement Methods in a Large-Scale Wave Basin

by

Matthew Robert Rueben


A PROJECT

submitted to

Oregon State University

University Honors College


in partial fulfillment of
the requirements for the
degree of

Honors Baccalaureate of Science in Mechanical Engineering (Honors Scholar)


Presented May 15, 2013
Commencement June 2013

Honors Baccalaureate of Science in Mechanical Engineering project of Matthew Robert
Rueben presented on May 15, 2013.

APPROVED:


_____

Mentor, representing Coastal & Ocean Engineering


_____

Committee Member, representing Geology & Geophysics


_____

Committee Member, representing Coastal & Ocean Engineering


_____

Head, School of Mechanical, Industrial and Manufacturing Engineering


_____

Dean, University Honors College




I understand that my project will become part of the permanent collection of Oregon State
University, University Honors College. My signature below authorizes release of my project
to any reader upon request.




_____

Matthew Robert Rueben, Author

# ACKNOWLEDGEMENTS

The completion of this thesis is a testament to the help and support extended to me during my undergraduate studies here at Oregon State University. Project-specific acknowledgements, both to fellow researchers and to funding sources, are made in the individual manuscripts. Several individuals went unmentioned in the manuscripts, however, that were key to the greater success of this research and to my development as a person.

My research mentor, Dr. Dan Cox, was perhaps the greatest contributor to my success. Over four years of regular meetings, he taught me how to direct my research wisely as well as how to present it clearly – and especially visually – to others. Moreover, Dan showed special interest in my future, even after graduation. He spent considerable time counseling me as I applied to graduate programs, and many of my key career decisions during that time were informed by Dan's experience-laden advice. I am very grateful to Dan, then, for his kindness toward me and for his investment in my goals.

I also want to thank my family, close friends, and God for supporting and guiding me through these past four years. My parents gave me constant encouragement as well as a humble appreciation for the privileges and opportunities I received through this research. My brother, Jacob, has blessed me with his shared enthusiasm for the intellectual intricacies of image analysis, and our late-night talks were a source of joy. I'm also grateful to my friends for showing such interest in my work, and to anyone willing to attend my defense so early in the morning. Without God, however, none of this work would be possible; only now do I recognize His purpose behind these four years of research, always moving me toward His calling for the rest of my life.

# CONTRIBUTION OF AUTHORS

Rob Holman oversees the Coastal Imaging Lab (CIL) here at OSU, which is where I began developing the wave edge tracking algorithm. Rob's connection to the Argus program and knowledge of optical measurement techniques was invaluable for designing the experiments presented herein. A notable example of Rob's contribution is the novel paint color scheme used on the debris specimen box lids in the 'Housesmash2' experiment.

John Stanley has authored and maintained much of the software surrounding the Argus Database, which handles operations like image rectification and merging for the Argus cameras used for this research. Image products from John's work provided a convenient basis for algorithm development, and his technical support was also helpful.

Dan Cox has provided research direction and advice as my mentor for the past four years. Dan served as the O.H. Hinsdale Wave Research Lab (HWRL) director during both experiments used in this study, and had a major role in experiment design. For the two manuscripts, Dan contributed research direction, significant refinement of all the figures, and a good deal of text for the Seaside paper.

Sungwon Shin was intimately involved with in-situ data acquisition and pre-processing for both experiments used in this study. Sungwon provided de-spiked in situ data and helped to establish time synchronization with the Argus cameras.

Jason Killian managed the HWRL facilities throughout this study. He was also involved with much of the camera setup for the wave basin, and helped me with camera calibration, geometries, and video acquisition.

# TABLE OF CONTENTS

# LIST OF FIGURES

# LIST OF FIGURES (Continued)

# LIST OF FIGURES (Continued)

# LIST OF TABLES

# Describing Tsunami Inundation and Debris Motion using Optical Measurement Methods in a Large-Scale Wave Basin

## Introduction

Novelty in scientific research often manifests as a unique pairing of method with topic, of which this thesis presents a clear example. Namely, this work applies promising optical measurement methods to a topic of recent international interest, that of overland flow during a tsunami. Cameras are well suited for measuring tsunami inundation in particular because a tsunami wave moves over a broad, roughly flat area that can be observed from a distance. Increasingly, cameras have large, color resolutions and high frame rates, even at low cost and compact sizes. The most exciting aspect of this work, however, is the aforementioned novelty of using cameras to learn about tsunamis. Each camera pixel can be treated as a separate instrument that, either individually or collectively, gives a completely different flavor of information about an unfolding tsunami experiment. Just one example of the singular conceptual difference will suffice: whereas in situ instruments give quantitative flow data that is laborious to conceptualize mentally, optical instruments give both quantitative and qualitative data simultaneously, parallelizing measurement and synopsis. Put simpler, the same video could both summarize an experiment to the uninformed observer and measure the wave speed, debris positions, and so on. Examples of this dual utility, shown in the body of this work, will prove this concept to be tremendously useful as even a starting point for research, with in situ instrumentation occupying only a secondary role as the provider of more detailed information on such-and-such a region identified in such-and-such an image.

Studying the effects of tsunamis has become of special concern considering the recent tsunami disasters around the world. For example, the tsunami that struck Tohoku, Japan on March 11, 2011 originated from a magnitude 9.0 earthquake off the Japanese coast and resulted in over 15,000 deaths (Mori et al., 2011). As for the future, the Cascadia subduction zone (CSZ) in the US Pacific Northwest has an estimated 14% chance of causing a 9.0 magnitude earthquake in the next 50 years (Groat, 2005).  This event would likely trigger a 10 m high tsunami that would hit the coast in approximately 30 minutes (USGS 2006). The size and speed of such a tsunami stresses the importance of studying tsunami-related hazards to reduce fatalities and damage. Two aspects of this threat are studied in this work: tsunami inundation and debris motion. The latter focus was inspired by the recent investigation of the Chilean Earthquake and Tsunami by Takahashi et al (2010), which stressed the importance of debris, particularly shipping containers, in contributing to the tsunami damage of coastal cities.  Other works address debris-structure impact in particular, while this research focuses on the free movement of the debris and the surrounding water.

This thesis consists of two separate manuscripts that address both of these aspects via laboratory experiments conducted at the O.H. Hinsdale Wave Research Lab (HWRL) at Oregon State University. The first manuscript centers on the 'Seaside' experiment of 2008, while the second uses the 'Housesmash2' experiment of 2010. Methodology and topic shift slightly between the two papers. The 'Seaside' paper develops a wave edge tracking algorithm to measure tsunami flow through an idealized urban waterfront. The 'Housesmash2' paper develops a debris tracking algorithm to measure the motion of multiple debris specimens. Special attention is given to repeatability and robustness for both algorithms, and their usefulness and drawbacks are discussed. As part of the NEES program, the data from both experiments are available to other researchers now that the

projects are concluded (e.g., Baldock et al., 2009), so this work can be repeated, expanded, and even improved upon in future studies.

The two goals of this thesis are, first, to develop novel, optical techniques for measuring otherwise impenetrable tsunami-related phenomena and, second, to provide research conclusions for practical application to tsunami preparedness efforts. These goals are both addressed within each individual manuscript. The 'Seaside' manuscript presents measurements of complex flow around groups of buildings, a difficult task both for in situ instruments and for numerical modeling. The results from this methodology illuminate general trends based on regional zoning (building size, density, etc.) and inform tsunami evacuation planning for the city of Seaside, Oregon. The 'Housesmash2' manuscript presents measurement and synoptic visualization of debris motion for multiple specimens simultaneously. The resultant data set could serve as a benchmark for developing tsunami debris transport models with the larger goal of predicting debris impacts and blockages from a damage mitigation and emergency response perspective.

# Optical measurements of tsunami inundation through an urban waterfront modeled in a large-scale laboratory basin

M. Rueben, R. Holman, D. Cox*, S. Shin, J. Killian, J. Stanley

Oregon State University, Corvallis, Oregon 97331 USA

*corresponding author: dan.cox@oregonstate.edu

## Abstract

This paper presents optical measurements of tsunami inundation through an urban waterfront in a laboratory wave basin. The physical model was constructed at 1:50 scale and was an idealization of the town of Seaside, Oregon. The fixed-bed model was designed to study the initial inundation zone along an urban waterfront, such that the flow around several large buildings could be observed. This paper presents an analysis of the optical measurements made with two overhead video cameras, focusing on tracking the leading edge of the tsunami inundation through the urban waterfront and quantifies the accuracy of the algorithm used to track the edge. The results show that the methodology provides high-resolution information in both time and space of the leading edge position, and that these data can be used to quantify the influence of large macro-roughness features on the tsunami inundation processes in laboratory settings. The overall effect of the macro-roughness was to decrease the bore propagation speed relative to the control section with no macro-roughness. The bore speed could be reduced by as much as 40% due to the presence of the macro-roughness relative to the control section.

## Keywords

Tsunami, laboratory experiments, macro-roughness, optical measurements, Argus, inundation, overland flow, urban waterfront, tsunami mitigation

## 1. Introduction

During the last decade, tsunami inundation modeling methods have evolved into mature numerical techniques, capable of simulating tsunami runup for complex, three-dimensional shoreline topography. Examples of current models include COMCOT (Cornell Multi-Grid coupled Tsunami Model) (Liu *et al.* 1995), MOST (Method of Splitting Tsunami) (Titov and Synolakis 1995), COULWAVE (Cornell University Long and Intermediate Wave Modeling) (Lynett *et al.*, 2002), STOC (Storm surge and Tsunami simulator in Oceans and Coastal areas) (Tomita and Honda, 2007), as well as the work by Grilli et al., 2007, Roeber et al., 2010, and many others. Since the 2004 Indonesia tsunami, there has been a significant increase in tsunami model research, particularly at the ocean-basin scale. But fewer models are capable of handling complex overland flows (Lynett 2007), and the flow around groups of buildings (Tomita *et al.* 2006) remains an active area of research.

The need for physical model data poses corresponding questions about how to make accurate measurements of the free surface and velocity in such a complex domain, especially given the interest in the details of inundation variability around macro-roughness. Since the location of the advancing inundation front is a primary variable of interest and since this front is clearly visible to the human eye, it seemed logical to investigate the potential of optical measurement methods. Thus, an important component of this work was the development and testing of these methods in a laboratory physical model environment.

This paper is outlined as follows. Section 2 presents the large-scale, hydraulic model basin, equipment, and rationale for the experimental setup and conditions. Section 3 presents the optical measurements, camera resolution, and details of the absolute measurement accuracy. Section 4 presents an analysis on the optical measurements, focusing on tracking

the leading edge of the tsunami inundation through the urban waterfront and quantifies the accuracy of the algorithm used to track the edge. This section also highlights features of the flow field that can be extracted from the optical measurements by tracking transects of image intensity sequentially in time. Section 5 concludes the paper by providing a concise summary of the main findings of the work.

## 2. Facilities, Equipment, and Experiment

The hydraulic model was designed to study tsunami flow over and around macro-roughness to observe the role, for example, of building shape and density on tsunami inundation and to develop a data set for the evaluation of the next generation of numerical models. Unlike previous hydraulic model studies that focused on the maximum extent of tsunami inundation and were often conducted on a scale of 1:200 or smaller, this fixed-bed experiment focused on the initial inundation zone along an urban waterfront such that the flow among several individual buildings can be observed. The model, constructed at 1:50 scale, was an idealization of the town of Seaside, Oregon, located in the Pacific Northwest of the United States (Fig 1). This location was chosen for several reasons. First, the constructed environment (seawall, hotel, residential and commercial buildings) were typical of coastal communities at risk to tsunamis with populations concentrated within the first 200 m of shoreline. Second, the bathymetry at Seaside was fairly easy to construct with uniform, shore-parallel contours and a relatively flat spit on which the buildings were constructed. Third, the USGS report (USGS 2006) gave reasonable guidance for the expected tsunami height triggered by a Cascadia Subduction Zone event (Fig 1).

The idealized bathymetry was shore parallel consisting of a constant depth section near the wavemaker, a 1:15 rise followed by a mild 1:30 slope, leading to another flat section on which the roughness elements were added (Fig 2, Fig 3). The bathymetry was constructed of smooth concrete with a float finish, and the roughness height is estimated to be 0.1 – 0.3 mm. In the real town, the hotels along the beach were fronted by an approximately 2 m high seawall in the center and dunes further to the north and south. The seawall was idealized in the model as 4 cm high, alongshore uniform, and the effects of the dune were studied separately. Eight large hotels and five large commercial building were constructed and sited based on aerial images and field surveys. The largest structure was a modern, eight story, u-shaped condominium in the center of the beachfront with a five story parking garage behind. The remaining buildings were other light commercial buildings, idealized as a square, and residential buildings, idealized as a smaller rectangle with pitched roof. The individual macro-roughness units were color coded with blue for large hotel or commercial building, red for smaller commercial buildings, and yellow for residential structures (Fig 2, 3). All elements were fixed in place to allow repeated runs of the experiment with the same macro-roughness conditions, and a LIDAR survey was taken to quantify the location of all the roughness elements to construct the boundary conditions for numerical models (e.g., Cox *et al.*, 2008). The Necanicum River which flows through the center of the city approximately parallel to the beach crest (Fig 1) was not modeled for this experiment, although the position of the river was painted with a light blue color (x=42 m) on the model for reference (Fig 3). Similarly, the positions of the city streets were painted black and included only as reference. The model did not include effects of vegetation, small-scale roughness, debris or sediments.

The tests were conducted in the Tsunami Wave Basin at the O.H. Hinsdale Wave Research Laboratory, Oregon State University. The basin was a rectangular box, 48.8 m long by 26.5

m wide by 2.1 m high.  The coordinate system for this experiment is shown in Fig 3, with x

positive onshore and x=0 at the rest position of the wavemaker, z is positive up with z=0 at

the flat bottom of the basin, and y is positive to the south with y=0 along the centerline of

the basin.  The basin was equipped with a segmented, piston-type wavemaker with a

maximum stroke of 2.1 m and maximum velocity of 2.0 m/s that was specifically designed

to generate precise, long waves for tsunami research. The tsunami inundation test program

consisted of  a wavemaker input signal constructed as a single positive surge using an error

function designed to maximize the full, 2.0 m stroke of the wavemaker with a stroke

duration of 10.0 s, producing a nominal wave height of 20 cm in the constant depth section

of the basin.  At prototype scale, the characteristic wave height corresponded to the 10 m

tsunami height estimated for the "500-yr" Cascadia Subduction Zone tsunami for this region

(USGS 2006). This input was repeated 136 times, with three pairs of co-located free surface

and velocity sensors moved along transects corresponding to major streets, and a fourth

pair was moved independently to one of four locations to extract turbulence estimates in

the wake of roughness elements (Cox *et al.*, 2008). Examples of wavemaker time history

displacements and resulting wave elevations are given in Fig 4 a and Fig 4b of Baldock *et al.*

(2009) which investigated the kinematics of breaking tsunami wavefronts using the same

facility and bathymetry configuration. A limited number of solitary wave runs at wave

heights ranging from 0.10 to 0.50 m and some impulse-type waves based on the error

function were run to evaluate the effect of the seawall and are not reported here.

It is worth noting that Madsen *et al.* (2008) provide an important discussion on the relevant

geophysical time and length scales for tsunamis, questioning the validity of the solitary

wave paradigm for tsunami research.  We agree with their assertion that the solitary wave

paradigm can be problematic, especially in terms of the length (or inundation time for our

work) of tsunamis created in hydraulic laboratories using solitary wave algorithms (e.g.,

Goring 1978). It is for this reason that we favored using the error function method to maximize the stroke of the wavemaker, producing a longer inundation time than would have been possible with a solitary wave of the same wave height. For our case, the nearshore wave propagation and inundation time was on the order of 30 s for our 1:50 scale tests and correspond to 210 s (3.5 min) at prototype scale, which is smaller than the 10-15 min time scale for a typical tsunami inundation (see Madsen *et al.*, 2008). Furthermore, no attempt was made to model the disintegration of the long wave into a series of shorter waves as described in their paper. Instead, the experiment focused on the inundation of a bore around idealized roughness elements modeled at length scales appropriate for an urban waterfront. Despite the shortened inundation time for the hydraulic model test relative to prototype tsunami conditions, the influence of macro-roughness in the urban waterfront is apparent in the leading edge and other details of the flow during the inundation process as will be shown in this paper.

To develop a comprehensive data set, several in-situ measurements were made where the measurement locations are shown in Fig 3 and representative times series from Trial 99 are shown in Fig 4. The paddle time history and water level on the paddle was recorded for each trial and used for synchronization (Fig 4a), where t=0 corresponds to 10 seconds before the start of the wavemaker. Four surface piercing wire resistance wave gages (WG) were fixed in the basin at the following x, y locations: WG 1 (2.086 m, -0.515 m), WG 2 (2.068 m, 4.065 m), WG 3 (18.618 m, 0.000 m), WG 4 (18.618 m, 2.860 m) as shown in Fig 3. The free surface time series are shown along the centerline for WG 1 over the flat section near the wavewamaker and for WG 3 near the start of the 1:30 slope prior to breaking (Fig 4b). WG 1 shows that the waveform is a fairly symmetric positive surge of water with a slight tail for t > 17 s, and WG 3 shows that the wave shape is asymmetric and pitched forward as the wave shoals over the 1:30 slope. The reflected wave can also been seen in

WG 3 for t > 34 s as a series of smaller waves. Four pairs of co-located ultrasonic wave gages (USWG) and acoustic-Doppler velocimeters (ADV) numbered 1 to 4 from north to south (positive y direction) were positioned among the roughness elements and moved to 10 different locations during the experiment with several repetitions at each location (Cox et al., 2008). Representative time series from Trial 99 are shown for the instantaneous free surface relative to the level of the fixed bed (Fig 4c) and the horizontal velocity (Fig 4d) for the first and second pairs.

## 3. Optical Measurements and Absolute Measurement Accuracy

As discussed in the introduction, the aim of this paper is to show the utility of optical measurements for tsunami inundation research using two Argus cameras mounted directly over the wave basin. This installation was one of the first applications of Argus collection hardware and methods, usually applied only to field site monitoring (Holman and Stanley 2007), to a physical model in a laboratory setting. The cameras (denoted Camera 7 and 8 following the naming convention for the 10 Argus cameras at the laboratory) were Scorpion FireWire imagers featuring 1280x960 pixel, 8-bit, Bayer-encoded CCD sensor chips and 4.5mm lenses spanning a 69° horizontal field of view. Images were RGB format and could be transformed to grayscale for processing. Camera lenses were calibrated for lens distortion prior to installation and the geometry of camera aim was found after installation by accurately determining the image location of known ground control points (GCPs) in each image (Holman and Stanley 2007). The two cameras were synchronized, and the corresponding images were rectified to the known elevation of the Seaside model (z = 1 m above the wave basin floor). The two images were then merged into single images (Fig 5) and serve as the basis of the research conducted for this paper.

Spatial resolution of the images is described by the footprint of pixels at each location. Figure 5 shows the resolutions in meters per pixel for the x-direction (cross-shore, left panel) and y-direction (alongshore, right panel). The spatial resolutions vary from 0.0095 m/pixel to 0.0148 m/pixel in the x-direction and from 0.0095 m/pixel to 0.0230 m/pixel in the y-direction. In general, optical measurements from these cameras were accurate to approximately 1 cm for most of the field of view.

Geolocation accuracy of imaged features also depends on stability of the ceiling camera mounts. Short term variations due to building vibration or wind response and long term variations due to thermal expansion or building creep can introduce error into assumed geometry solutions. Therefore, it was necessary to determine the stability of camera geometries and the effect on the absolute accuracy of pixel locations. A time stack (Holman and Stanley 2007) was created by taking a vertical and a horizontal transect through each of the unrectified images taken over a 60-day period. If the cameras were perfectly stable relative to the imaged surface, a vertical time stack would yield an image with horizontal bands. Fig 6 (left) shows a portion of an un-rectified image with the example slice indicated by the vertical line, and Fig 6 (right) shows a vertical time stack created from sequential images taken for the selected transect. The houses and commercial building from the image on the left appear in the time stack image on the right as shaded bands. In this example, there is an identifiable camera shift in the image after snapshot number 160.

In this manner, vertical and horizontal time stacks were created for each camera (four time stacks total) after eliminating images that had poor lighting or low average intensity values. Fig 7 shows the camera shift in pixels over the course of the experiment from February 15 to April 10, 2008, for Camera 7. The figure indicates that the Camera 7 was relatively stable throughout the experiment with shifts within ± 2 pixels. This translates to an absolute error

of approximately ± 2cm, although the relative error is lower (e.g., the relative position of the runup for a single event will have less than a 2 cm error).  One exception is in the vertical shift (Fig 8a) in Camera 7 after Yearday 90 where the shift was between 2 and 6 pixels, likely due to a gradual warming of the building.  The shift in Camera 8 was also within ± 2cm, and the gradual shift after Yearday 90 was not observed (figure not shown for brevity).

## 4. Analysis of Optical Measurements

For this paper, four regions of interest, denoted A-D, were selected to represent (A) the control region for which there was no macro-roughness, (B) a region with a waterfront hotel typical of that area backed by residential buildings, (C) a city street running parallel to primary flow direction and flanked by hotels on the waterfront, and (D) a commercial area with a large hotel backed by other large structures representative of commercial areas (Fig 8).  Regions B, C, and D are fronted by a low seawall described earlier, and Region A (the control) is not.  A thin (2 cm) divider wall separated the two regions.  As will be discussed later, Regions A-D in Fig 8 refer to regions several pixels in width to provide an average of the tsunami bore propagation (Fig 15) and Transects a-d refer to particular vectors of pixels within the region (i.e. one pixel width). Note that the test regions indicated in Fig 8 are in the areas of high resolution (less than 0.01 m/pixel) shown in Fig 5, with the exception of the relatively stable Region A (control).

Analysis of the image data required measurement of a reliable set of wave edge positions due to the tsunami inundation for each image.  In theory, this would be a simple task if the leading edge of the tsunami front were brighter (higher image intensity) than the rest of the image. Unfortunately, this was usually not the case, particularly due to the large turbulence

generated by the flow through the macro-roughness and the relatively thin film at the leading edge (e.g., Fig 11, left). Therefore, it was necessary to develop a more sophisticated method to identify the leading edge of the tsunami bore.

The first step in isolating the wave edge was to convert the frames from RGB color images to intensity images, assigning each pixel a scalar value that represents its overall brightness, instead of the three values (red, green, and blue) required for color images. Next, a reference image for which the wave was not present was subtracted from each video frame, forming a difference image. These difference images isolate the fluid motion from pixels that are otherwise bright but are unchanging. Fig 9 (left), for example, shows a difference image from Trial 80 at t=24.06 s where the lighter shades indicate wave breaking and turbulence. By comparing with Fig 8, it can be seen that bright buildings and overhead lights (appearing as an array of bright spots throughout Fig 8) have been essentially eliminated. Fig 9 (right) shows a difference image for the same run taken at t=27.26 s during the inundation phase. The figure clearly shows that the optical system captures complexities of the flow field around the macro-roughness elements which will be discussed in context with Fig 10. Note that the overhead lights along rows x=26.5 m and x=30.5 m add unwanted noise to the signal but are seaward of the inundation front so are of no consequence.

From the individual images, time stacks were constructed for each of the four transects a-d (Fig 10a-d). Before discussing edge detection, it is instructive to compare the signatures of the four time stacks shown in Fig 10. All four images show high intensity in the region 28 < x < 32 m for 23.5 < t < 25 seconds which represents the wave breaking process seaward of the macro-roughness. Although wave breaking is a continuous process, this breaking front does not advance steadily in the transition region (x=32 m). Continuing with Fig 10a, after

the broken wave is established as a quasi-steady bore, the bore advances over the flat, uniform slope at a nearly constant speed, inferred from the straight line of "x's" (detected edges; 26 < t < 30 s), until it reaches the back wall of the basin (x = 43 m). From the vertical back wall, the flow forms stationary bore (30 < t< 32 s) and then a seaward propagating bore, again at near constant speed, albeit slower than the incoming bore.  In contrast to the control transect, Transects b, c, and d all show a seaward propagating wave reflecting from the seawall and first row of hotels on the urban water front (27 < t < 32 s) which was also evident in the original images (see Fig 11).  The time stacks reveal that the propagation speed of the reflected wave is not uniform and increases as the wave travels to deeper water as expected from linear wave theory.  It is also interesting to note that the reflection happens over a finite time, approximately 1 sec (26 < t < 27 s), similar to the finite time required for the bore to reflect off the back wall in the control transect.

Landward of the hotels on the waterfront (x > 34 m), the time stacks in Fig 10b-d show significant differences in the inundation process owing to differences in macro-roughness. Fig 10b for the 'residential' transect shows an area of high intensity immediately behind a hotel (x =35 m) and is stationary with respect to time (27 < t < 29 s), suggesting that processes related to high Reynolds stresses such as sediment suspension and scour would be important in this region.  Fig 10c, the 'city street' transect, shows a region of high intensity at the urban waterfront (x=33.5 m) that is somewhat stationary for 26 < t < 27 s. This high intensity motion can also be observed after the passage of the front, either generated at the waterfront (x=33.5 m) and advected landward, or produced by wakes from roughness elements adjacent to the street, or both.  Fig 10d for the 'commercial' transect is also unique, with perhaps the most striking feature being the second reflected wave propagating from the face of the u-shaped condominium, i.e., the "bottom" of the u at x=35.5

m for 27 < t < 30 s.  One can also note that the detected edge is discontinuous owing to the presence of the large buildings.

The leading edge trajectory was tracked using time stacks as shown in Fig 10 along each vertical pixel vector for -7 < y < 6 m.  An algorithm was developed to detect the landward-most statistically significant bright point and then a polynomial curve was fitted to the raw edge, producing an initial estimate of the wave edge. The algorithm was repeated with lower brightness thresholds to refine these estimates. Examples of the final edge position are indicated by the x's in Fig 10 for the four transects.

As a representative example, Fig 11 (left) shows the estimated wave location (dot) for a single run (Trial 99) at one instant (t=26.3s) superimposed on the rectified image. The four triangles located between 34 < x < 37 m indicate the location of the in-situ sensors (co-located ADV and ultrasonic wave gage).  The panel on the right shows the time series from the wave gages at the four locations with the corresponding time of the left image shown by the vertical bar.  Comparison of the optical and in-situ data for this figure and similar figures for other locations of the in-situ sensors indicated that the arrival time of the bore predicted by the optical measurements coincides with the sharp increase in water level observed by the wave gages.  This provides further support that the bore tracking algorithm developed for the optical measurements gives an accurate estimate of the leading edge throughout the complex flow field.

Figure 12 shows the mean edge position over 21 trials at t=28.7s.  Inspecting the leading edge along the y-direction shows that the bore in the control region (x < -6 m) leads the edge everywhere in the macro-roughness region (-6 < x < 6 m).  The macro-roughness along the urban waterfront and in the residential and commercial areas reduced bore propagation speed significantly compared to the control region.  Also, there are several peaks (y= –3.1,

0.4, and 2.6 m) where the streets leading to the beach are unimpeded by hotels and other buildings, allowing the fluid to flow with less disturbance. Interesting, the peaks for the streets y = 0.4 and 2.6 m are larger than that at y = –3.1m, even though the latter two streets form an acute angle with the flow direction.  These two peaks are approximately the same as the peak at y= -6 m along the guide wall, suggesting that the large u-shaped condominium, adjacent parking structure and other buildings formed a 'channel', allowing the fluid to flow relatively unimpeded.  This is in contrast to the two streets at approximately y = 4 m and y = 5 m for which peaks in the edge do not occur.  Both of these streets also lead directly to the water front and form the same acute angle with the flow direction; however, the spacing of the macro-roughness in the domain 3 < y < 6 m, 35 < x< 37 m is such that large hydraulic jumps are formed on the seaward side of the roughness elements with large, turbulent wakes in their lee. Figure 13 shows a detail of the mean edge position over the 21 trials in the range -5 < y < -2 m at five times during the inundation process and shows how the macro-roughness retards the flow relative to the open street running parallel to the flow direction.  Taken collectively, Fig 10, 11, 12 and 13 show that macro roughness plays a significant role in the details of tsunami inundation.

The repetitive nature of the fixed-bed inundation study allowed for comparisons among the runs to quantify the repeatability of the tests and measurement technique.  Of the 136 runs, 21 were selected to test repeatability.  Although the cameras were synchronized to each other, they were not synchronized to the start of the wavemaker.  Therefore, a correlation technique was used to determine the lag between each run and a reference run to within 2 ms.  The edge position at each column transect in each frame was averaged across the 21 runs, yielding a mean and standard deviation value for each point. Fig 14 maps the standard deviation of the arrival time of the leading edge throughout the domain.  For most of the domain, the standard deviation of the bore arrival time is less than 0.2 s.  The errors in

arrival time increase with landward distance from the shoreline by as much as 1 s owing to the complexity of the flow in that region. Overall, Fig 9-14 show that the optical measurements yield accurate, quantitative, synoptic observations of tsunami inundation through macro-roughness in a large-scale hydraulic model facility.

Fig 15 gives an illustrative example of how the optical measurements can be used to compare the effects of macro-roughness on tsunami inundation.  The upper panel of the figure shows the wave edge position as a function of time, averaged for the 21 runs selected, over the four regions A-D shown in Fig 8, and the lower panel shows the first derivative in time (velocity of the leading edge).  As discussed in reference to Fig 10, all regions show a uniform motion seaward of the breakpoint ($x < 30$ m; $t < 23.6$ s), and the speed of the crest is nearly constant.  During the breaking process in the transition region, the bore speed decreases markedly ($30.5 < x < 31.5$ m; $23.7 < t < 24.3$ s) followed by an acceleration ($31.5 < x < 32.2$ m; $24.3 < t < 24.7$ s).  The four regions again show that the bore has a nearly uniform propagation speed ($32.2 < x < 33$ m; $24.7 < t < 25.1$ s) prior to reaching the urban waterfront.  Landward of the waterfront, ($x > 34$ m; $t > 25.3$ s), the control area Region A shows a near-uniform propagation speed over the  flat section ($34 < x < 42.5$ m; $25.3 < t < 28.7$ s), whereas Regions B-D show significant influence of the macro-roughness, consistent with the observations in Fig 10, and propagation speeds generally decrease relative to the control section.  For the control section, the propagation speed is 2.6 m/s on average for $34 < x < 38$ m, whereas the propagation speed reduces to 1.5 m/s on average for the residential section.  Therefore, the presence of the macro-roughness can reduce the inundation speed by 40%.  It is noted that the data have been deleted for Region D for $33.5 < x < 37.7$ m ($25.4 < t < 27.6$ s) corresponding to the large buildings where no fluid was present.

As expected, the road leading away from the waterfront (Transect C) has a greater

propagation speed than either then residential (B) or commercial (D) transects for the first

few city blocks (34 < x < 38 m).  It is somewhat surprising, however, that the bore speed

slows down considerably for x > 39 m and is eventually surpassed by the bore speed in the

commercial section.   In any case, the optical measurements are able to capture such

detailed features of the flow throughout much of the inundation area.


## 5. Conclusion

This paper presents optical measurements of tsunami inundation in a laboratory wave

basin.  The physical model was constructed at 1:50 scale and was an idealization of the town

of Seaside, Oregon, and this fixed-bed model was designed to study the initial inundation

zone along an urban water front, such that the flow around several large buildings could be

observed (Fig 4). The input signal for the wavemaker was based on an error function to

utilize the full stroke of the wavemaker (2.0 m) and produce a single positive surge with a

nominal height of 20 cm, corresponding to a 10 m prototype tsunami offshore, and was

used repeatedly for the data shown in Fig 9 – 15.  Two cameras were installed overhead as

part of the Argus network (Holman and Stanley, 2007).  The camera resolution was shown

to be less than 1 cm per pixel for most of the field of view for a given realization (Fig 5).  The

cameras were shown to be stable throughout the experiment, and minor shifting in the

images due to thermal expansion of the building accounted for a 2 cm shift in the absolute

error (Fig 7).  Overall, the Argus system was shown to be effective in quantifying various

aspects of the tsunami inundation process through the constructed waterfront.  Specifically,

1. Comparison of the timestacks in Fig 10 show that the macro-roughness represented by the constructed environment (Fig 10b,c,d) significantly impacts the tsunami inundation process relative to the control area (Fig 10a) without macro-roughness.

2. The overall affect of the macro-roughness is to decrease the propagation speed relative to the control section with no macro-roughness and can reduce the inundation speed by 40% relative to a control case.

3. The details of the macro-roughness have a significant influence on the tsunami inundation (Fig 10b,c,d; Fig 12; Fig 14).

Further research is needed to systematically quantify the influence of building shape and density on the tsunami inundation pattern. Moreover, these data can serve as a benchmark for tsunami inundation models. The data set comprised of LIDAR bathymetry, in-situ measurements of free surface and velocity, and Argus video is available by contacting the third author.

**Acknowledgements**

## References

Baldock, T.E., Cox, D. Maddux, T., Killian, J., Fayler, L. (2008) "Kinematics of breaking tsunami wavefronts: A data set from large scale laboratory experiments," *Coastal Engineering*, 56, 506-516.

Cox, D., Tomita, T., Lynett, P. and Holman, R.A.(2008). "Tsunami Inundation with Macro-Roughness in the Constructed Environment." *Proc. 31st International Conference on Coastal Engineering*, ASCE, 1421-1432.

Goring, D.G. (1978) "Tsunamis – the propagation of long waves onto a shelf," *REP Kh-R-38*, W.M. Keck Lab. of Hyd. and Water Resources, Calif. Inst. Technology., California.

Grilli, S. T., Ioualalen, M., Asavanant, J., Shi, F., Kirby, J. T., Watts, P., (2007) Source constraints and model simulation of the December 26, 2004, Indian Ocean Tsunami, *Journal of Waterway, Port, Coastal and Ocean Engineering*, Special Issue on Tsunami Engineering, 133, 6, 414-428.

Groat, C.G., (2005) Statement of C.G. Groat, Director, US Geological Survey, US Department of the Interior, Before the Committee of Science, US House of Representative, January 26.

Holman, R. A., and J. Stanley (2007) "The history and technical capabilities of Argus," *Coastal Engineering*, 54, 477-491.

Liu, P.L.-F., Cho, Y.-S., Briggs, M.J., Kanoglu, U. and Synolakis, C.E. (1995). "Runup of solitary waves on a circular island." *J. of Fluid Mechanics*, 302, 259-285.

Lynett, P., Wu, T.-R., and Liu, P. L.-F., 2002. "Modeling Wave Runup with Depth-Integrated Equations," *Coastal Engineering*, v. 46(2), p. 89-107.

Lynett, P.J. (2007) Effect of a Shallow Water Obstruction on Long Wave Runup and Overland Flow Velocity," *J. of Waterway, Port, Coastal and Ocean Engineering*, 133, 6, 455-462.

Madsen, P. A., Fuhrman, D.R., Schaffer, H.A. (2008) "On the solitary wave paradigm for tsunamis," *J. Geophysical Research*, Vol 113, C12012.

Tomita, T., Honda, K., Kakinuma, T. (2006) "Application of three-dimensional tsunami simulator to estimation of tsunami behavior around structures, *Proc. Int. Conf. on Coastal Engineering*, San Diego., Vol 2, 1677 – 1688.

Tomita, T. and Honda, K. (2009) "Tsunami estimation including effect of coastal structures and buildings by 3D model" *Proc. Coastal Structures '07*, Am. Soc. Civil Engineers, Vol 1, 681 – 692.

Titov, V.V. and Synolakis, C.E. (1995) "Modeling of Breaking and Nonbreaking Long Wave Evolution and Runup using VTCS-2," *J. of Waterway, Port, Coastal and Ocean Engineering.*, 121, 6, 308-316.

Riggs, H.R., Robertson, I.N., Cheung, K.F., Pawlak, G., Young, Y.L., Yim, S.C.S., 2008, "Experimental simulation of tsunami hazards to buildings and bridges," *Proc., NSF CMMI Engineering Research and Innovation Conference*, Paper No. 0530759.

Roeber, V., Cheung, K.F., and Kobayashi, M.H. (2010). Shock-capturing Boussinesq-type model for nearshore wave processes, *Coastal Engineering*, 57, 407-423.

USGS Tsunami Pilot Study Working Group (2006) "Seaside, Oregon Tsunami Pilot Study – Modernization of FEMA Flood Hazard Maps," *Open-File Report 2006-1234*. US Department of the Interior, US Geological Survey.

van de Lindt, J.W., Gupta, R., Garcia, R., and Wilson, J., (2008) "Tsunami bore forces on a compliant residential building model," *Engineering Structures,* (in press).

**Figures**



**Figure 1:** Google image of Seaside, OR with experiment model extents (dashed) and estimated tsunami inundation line (solid). **Inset:** Google image of Pacific coastline with Cascadia Subduction Zone (solid), NOAA DART buoy locations (triangle), and Seaside, OR (circle).

**Figure 2:** Photograph of Tsunami Wave Basin with tsunami inundation experiment based on idealized model of Seaside Oregon at 1:50 scale (center; Cox *et al.*, 2008). Basin hosted two other projects simultaneously: destructive testing for 1:6 scale tsunami-structure interaction (left; van de Lindt *et al.*, 2008) and Performance Based Tsunami Engineering project (right; Riggs *et al.*, 2008).
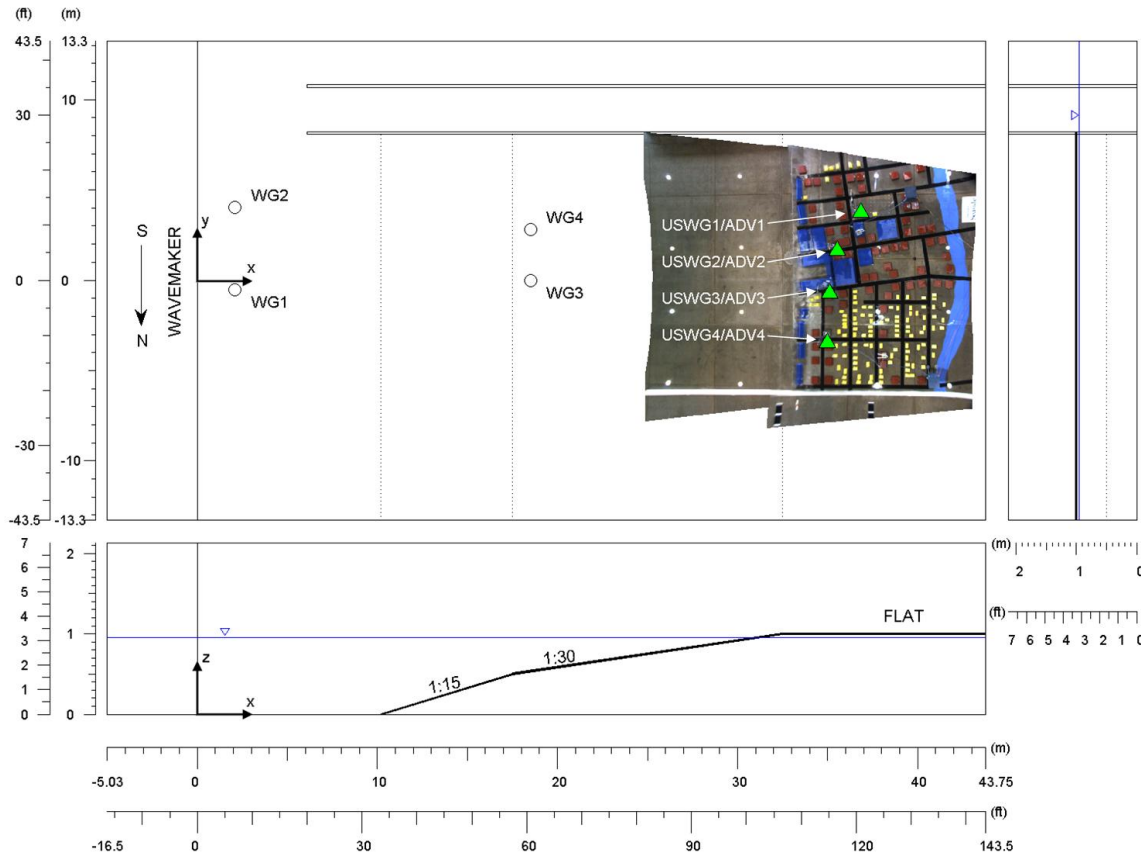
**Figure 3:** Orthographic view of the Tsunami Wave basin. Top left panel shows plan view of basin with Argus images from Cameras 7 and 8 superimposed. Bottom panel shows bathymetry and still water line.
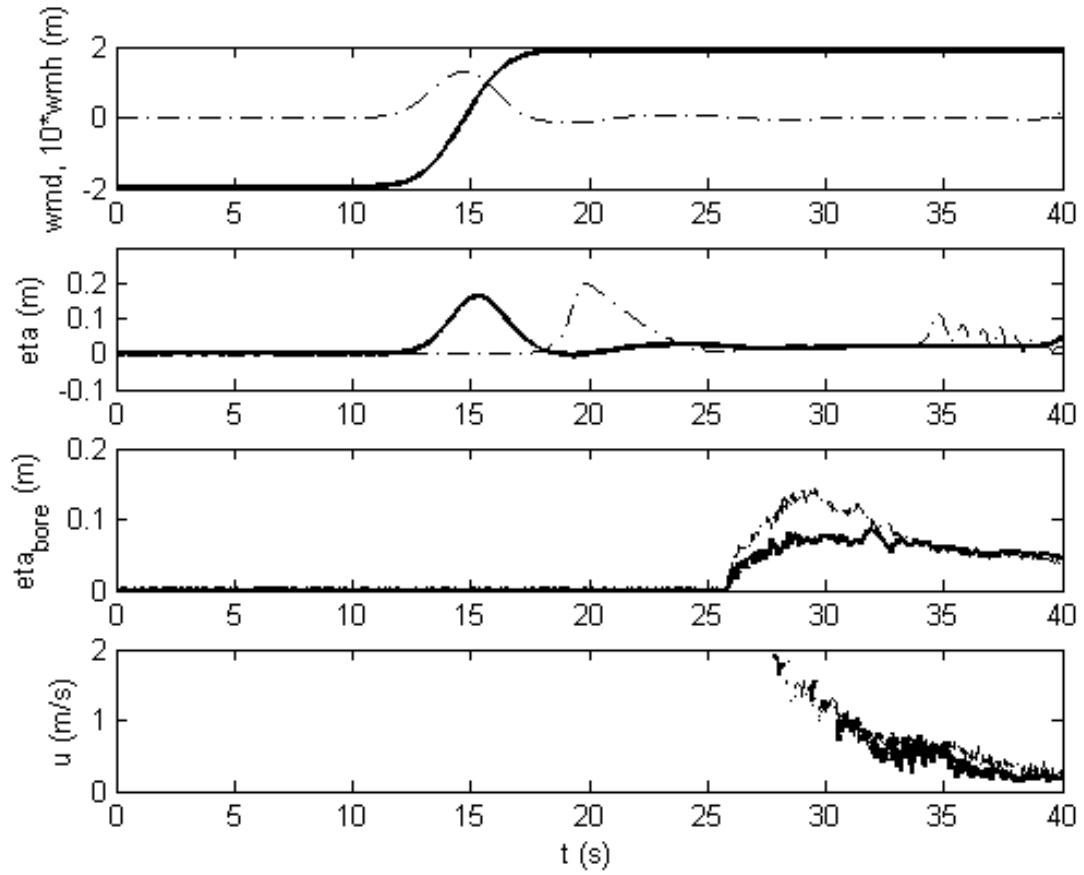
**Figure 4:** Time series of in-situ measurements showing (a) time history of paddle displacement (solid line) and water level on paddle (dash), (b) water level at WG1 (solid) and WG 3 (dash), (c) bore height above fixed-bed model using USWG1 (solid) and USWG2 (dash), (d) horizontal velocity measured by ADV1 (solid) and ADV2 (dash) for Trial 99.

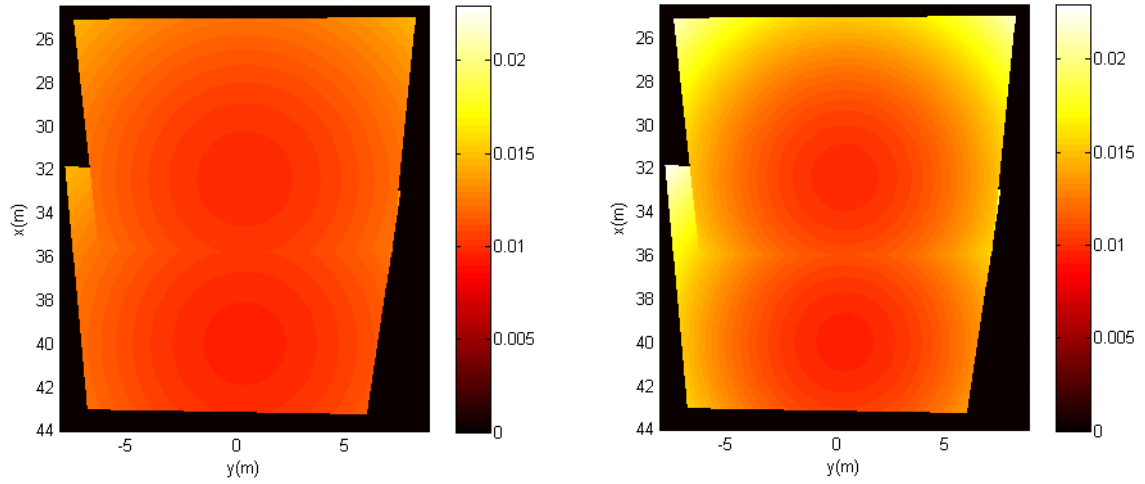**Figure 5:** Resolution of the rectified and merged images from Cameras 7 and 8 for the x-direction (left) and y-direction (right) with resolution scale in meters.
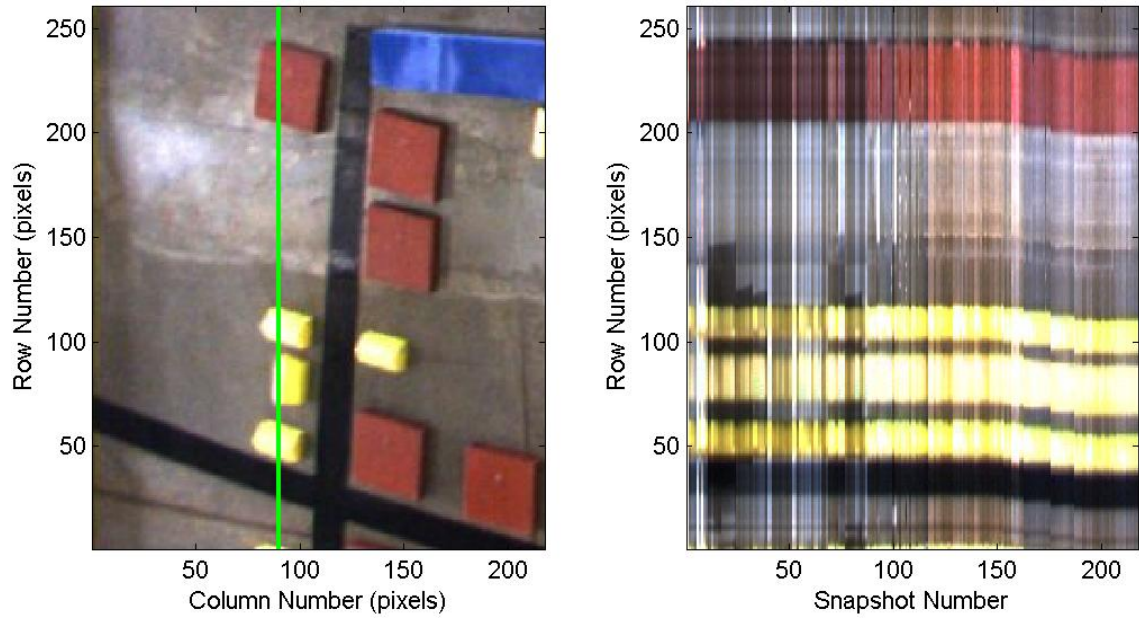
**Figure 6:** Portion of un-rectified image snapshot number 155 from Camera 7 taken on March 25th, 2008, at 22:05:00 GMT prior to run (left) and portion of column-wise time stack (right) using transect indicated by vertical line on left image.
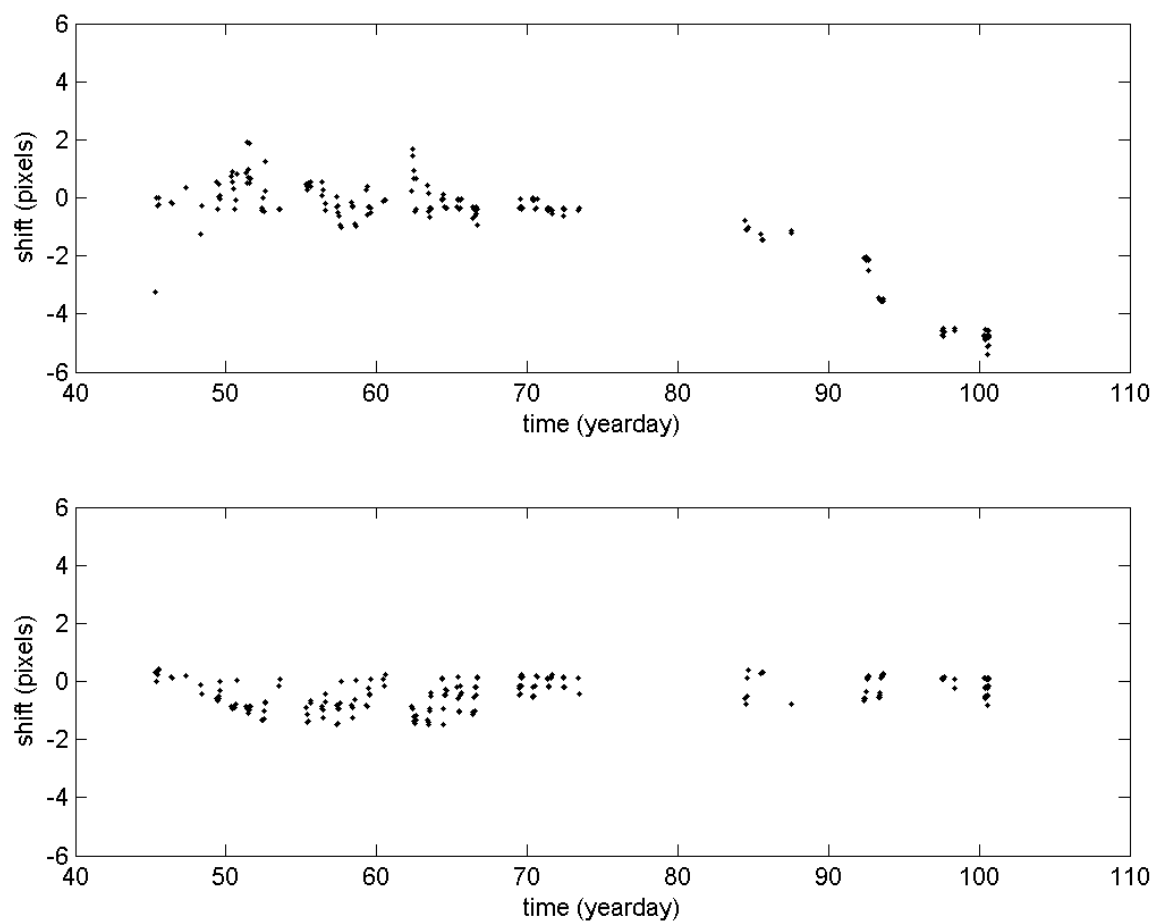
**Figure 7:** Pixel lag from February 15 to April 10, 2008, for Camera 7 columns (top) and rows (bottom).
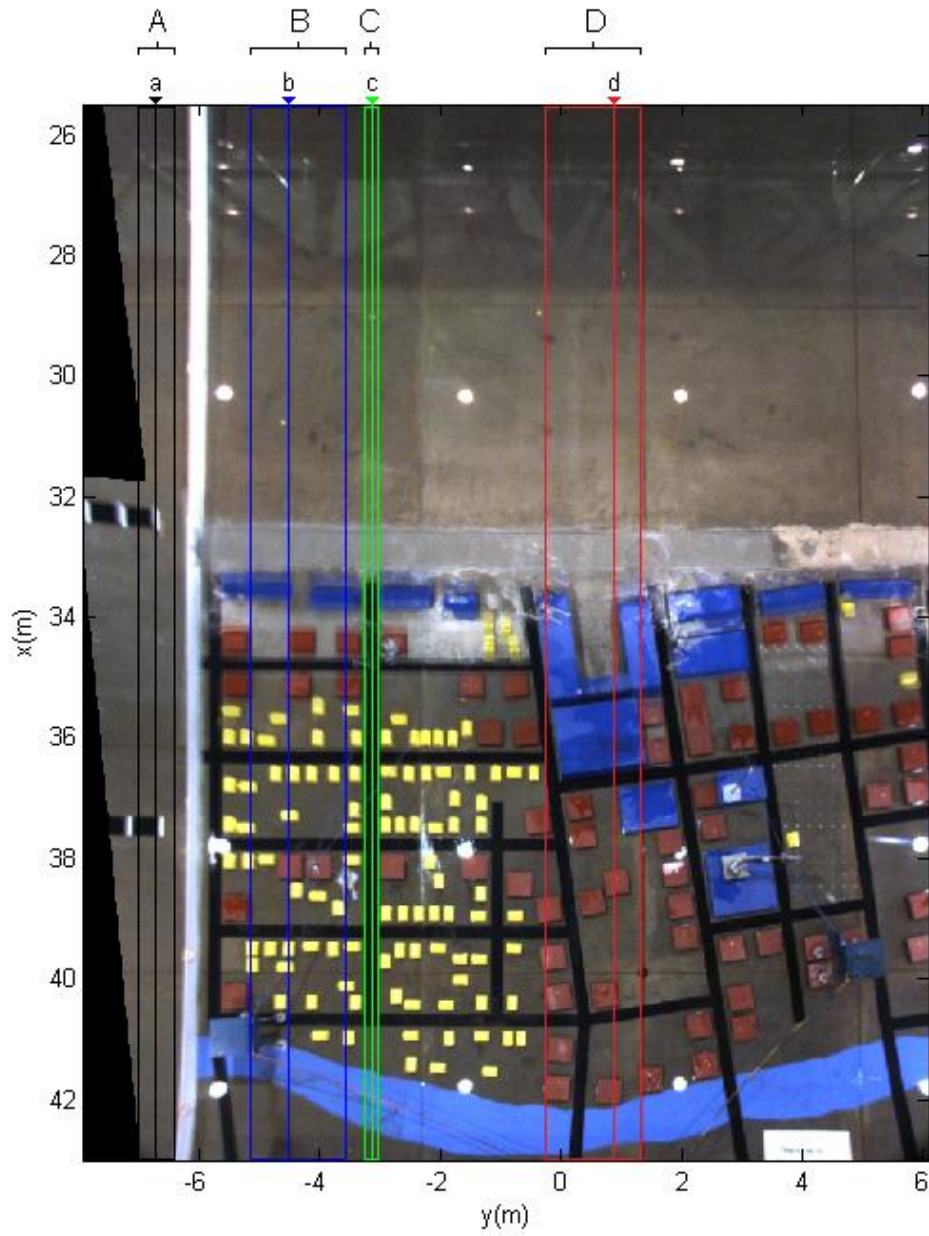
**Figure 8:** Rectified, merged, and cropped image from cameras 7 and 8. Regions ABCD refer to Figure 15 and Transects abcd refer to Figure 10.
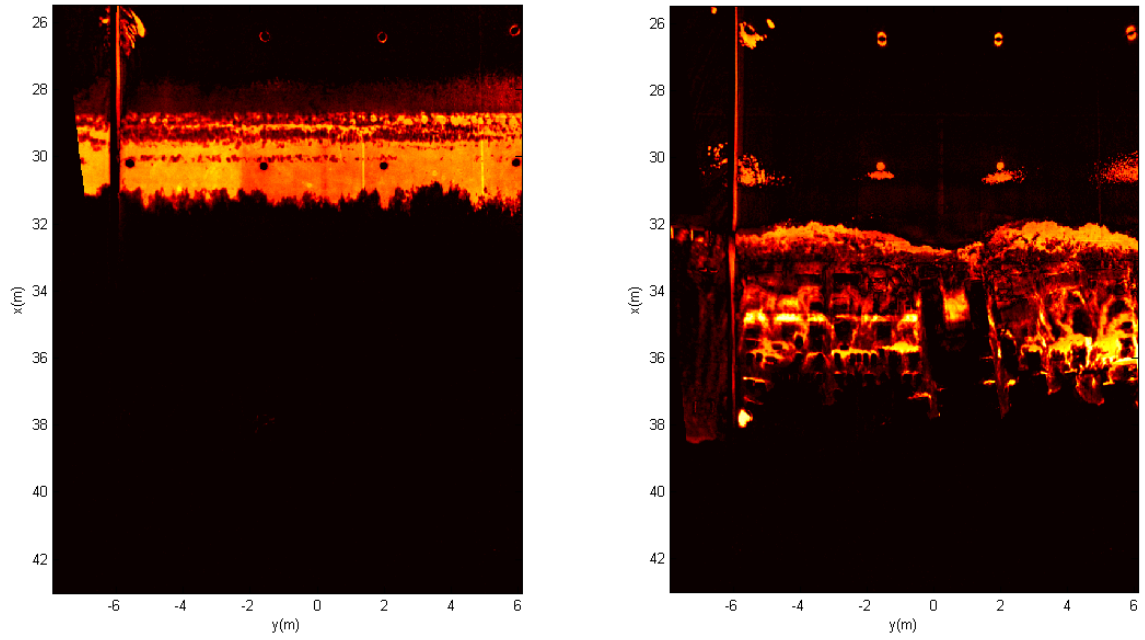
**Figure 9:** Difference images from Trial 80. Test images taken at t=24.06 s during wave breaking (left) and t=27.26 s during inundation (right).
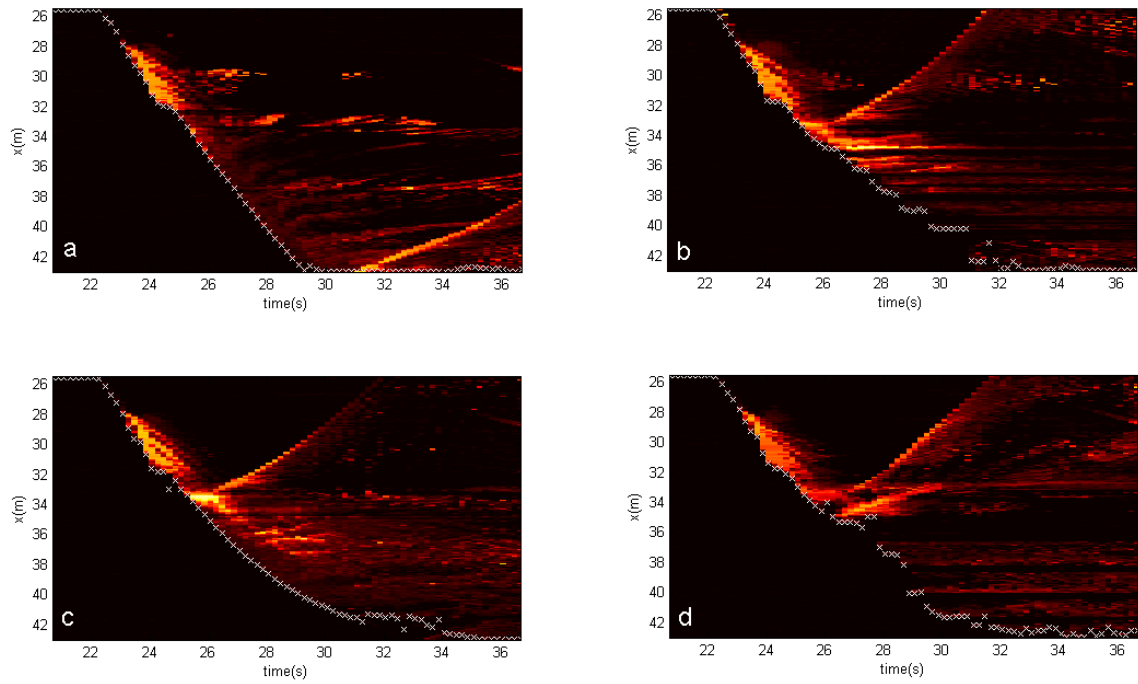
**Figure 10:** Time stacks of image intensity for Transects a (control), b (residential), c (street), d (commercial), where transect location is given in Fig 5. Shades represent relative intensities and are scaled the same as Fig 9.
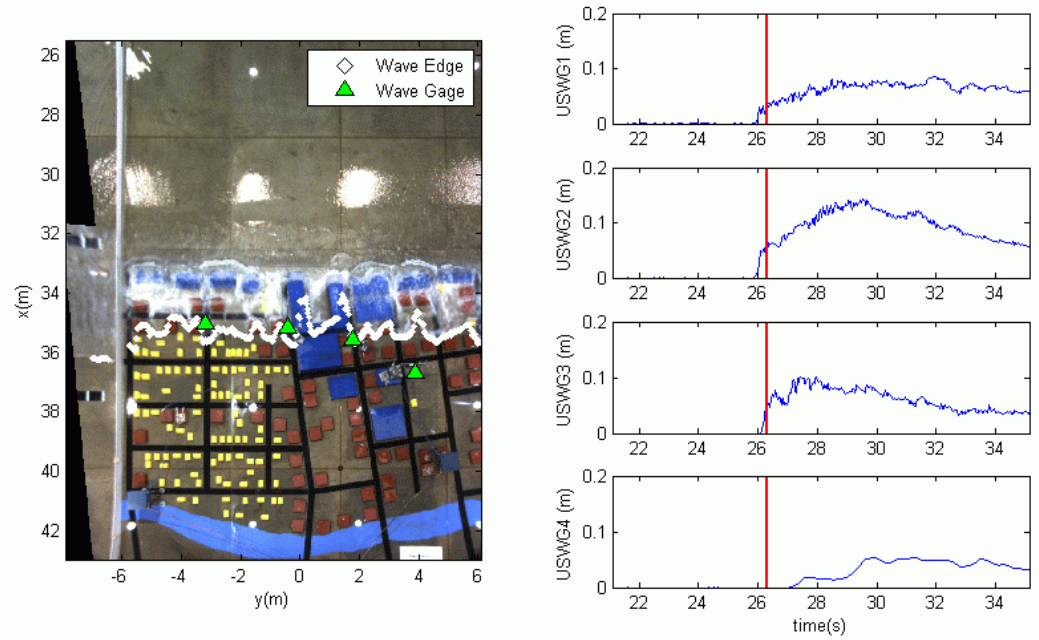
**Figure 11:** Left: Image from Trial 99 at t=26.3s with calculated wave edge (dot) and ultrasonic wave gage locations (triangle) superposed (note wave gages are numbered 1-4 from left to right). Right: Time series of in-situ free surface elevation with corresponding time for the left panel image indicated (vertical line).
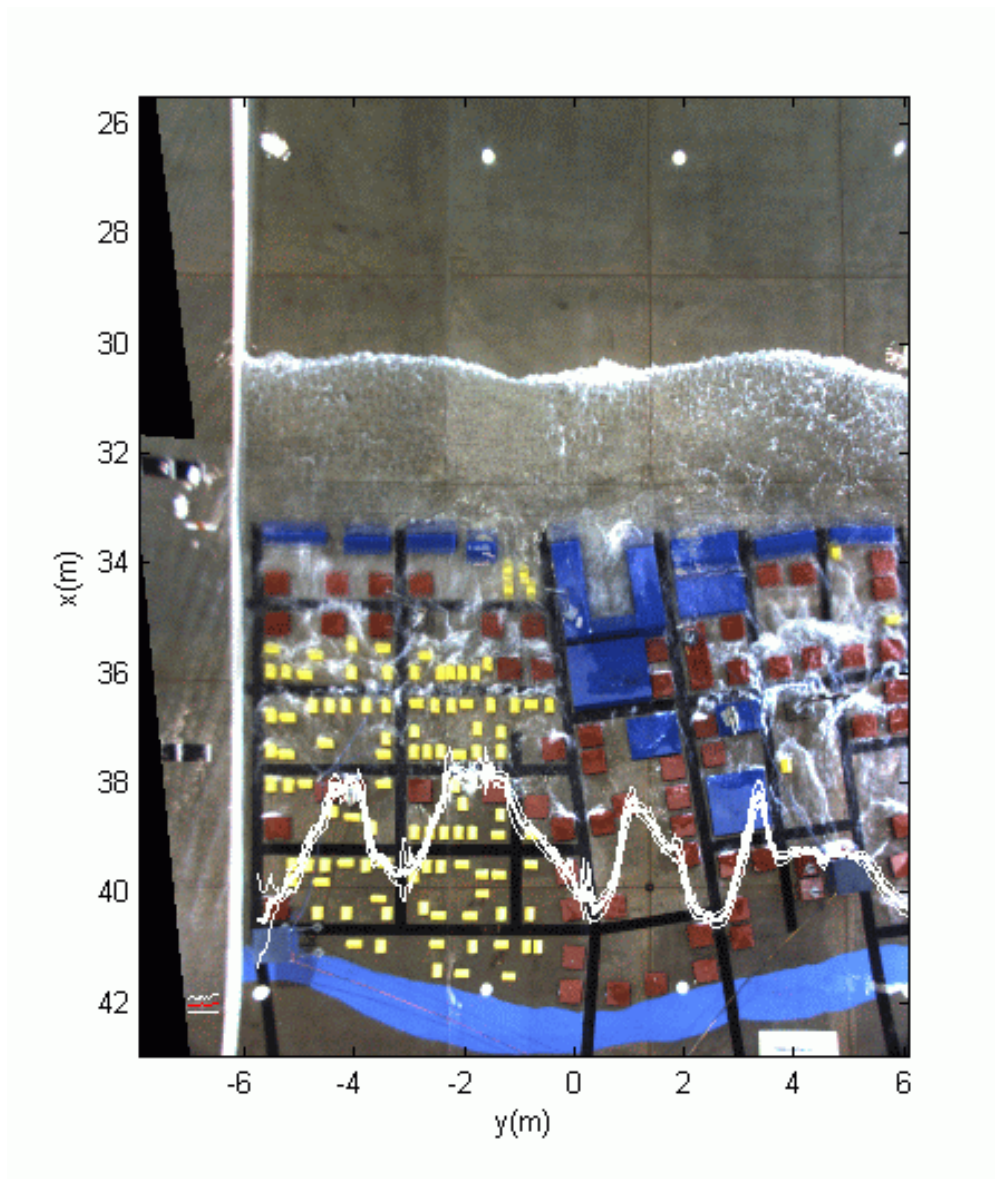
**Figure 12:** Mean edge position over 21 trials (heavy line) and standard deviation (light line) at t=28.7 s.
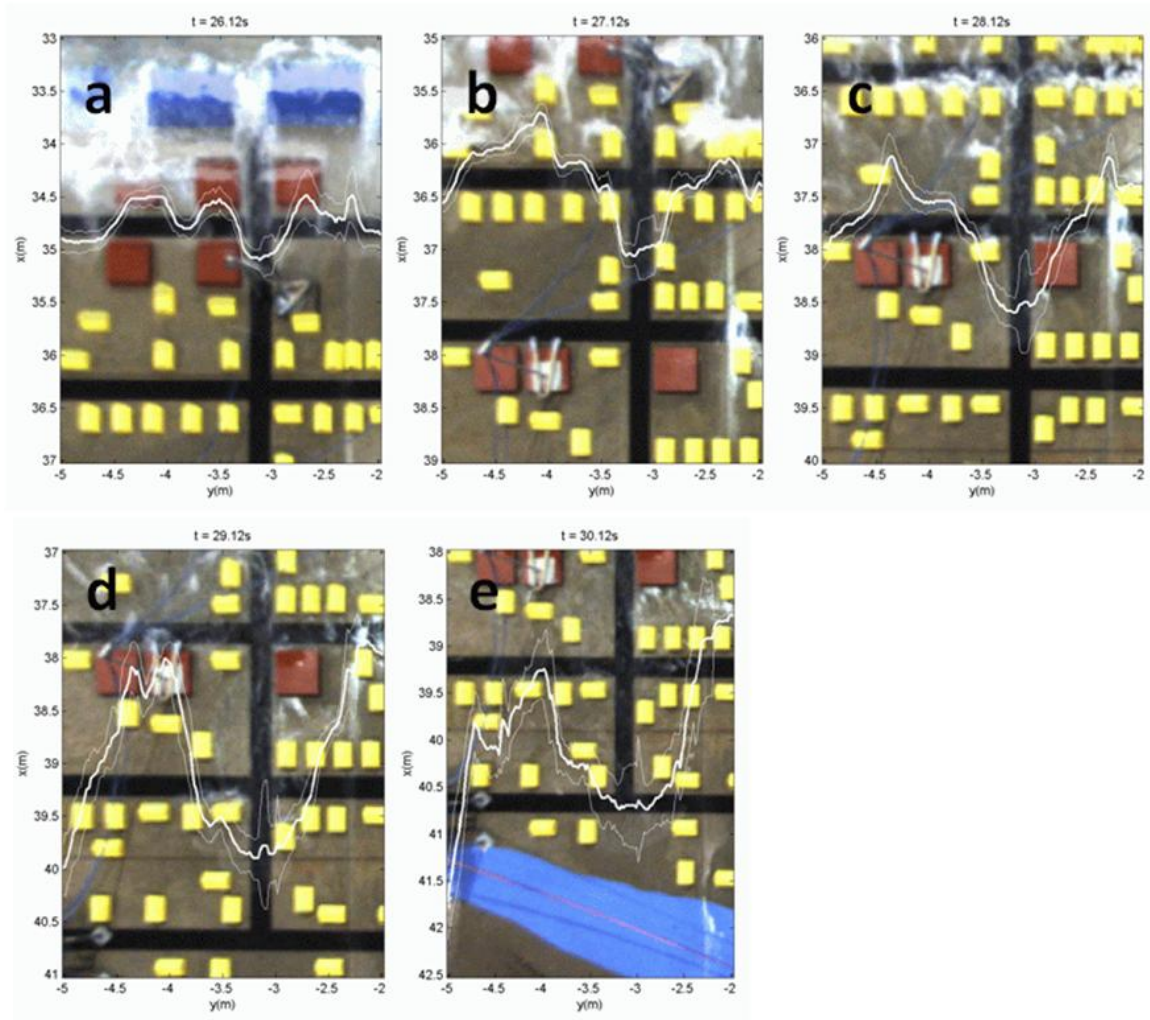
**Figure 13:** Detail of mean edge position over 21 trials (heavy line) and standard deviation (light line) in the range -5 < y < -2 m at (a) t = 26.12 s, (b) t= 27.12 s, (c) t=28.12 s, and (d) t=29.12 s and (e) t=30.12 s.
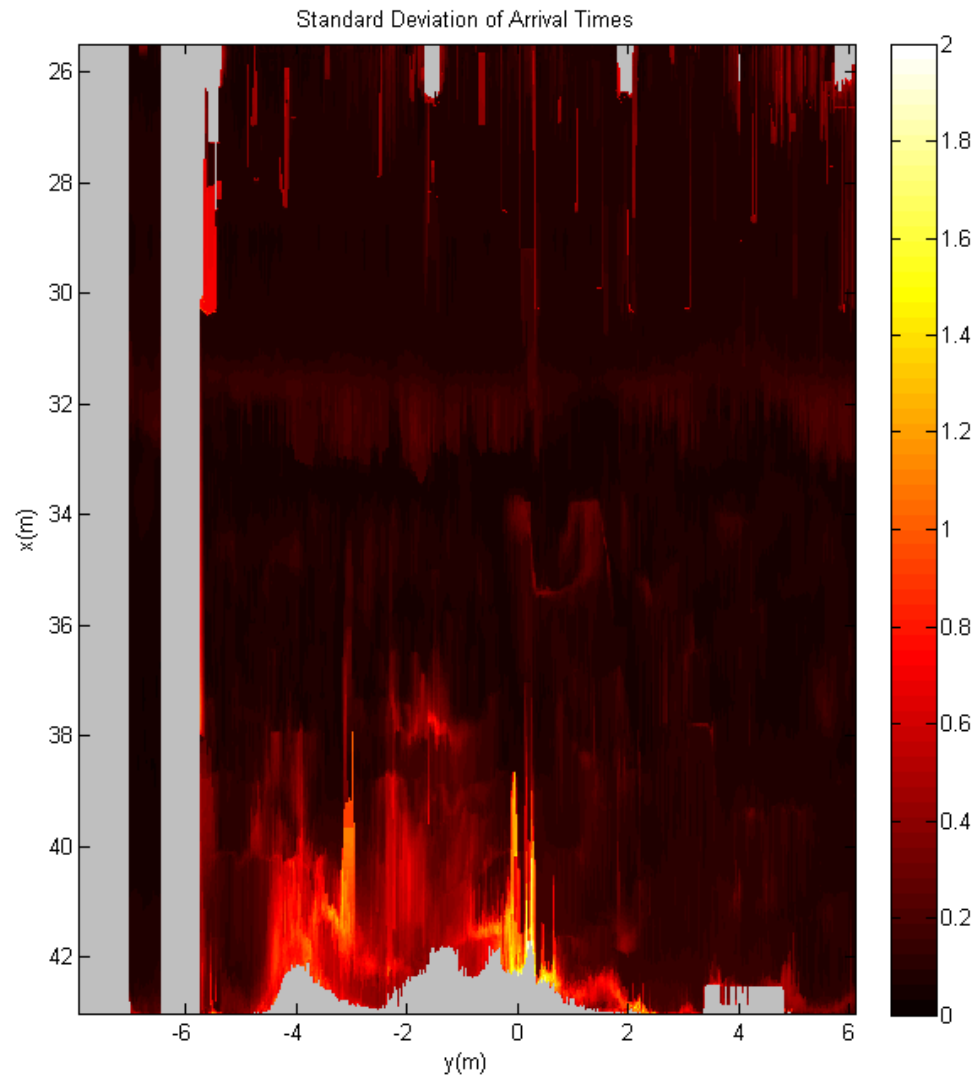
**Figure 14:** Standard deviation map of interpolated arrival times in seconds.
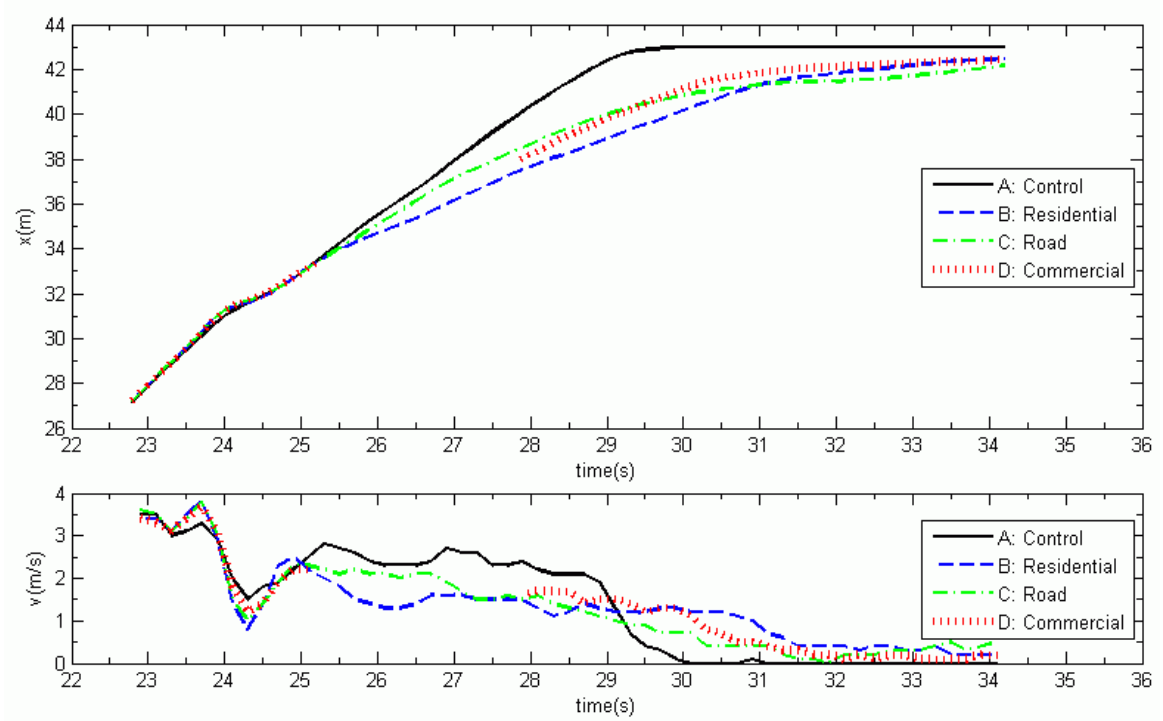
**Figure 15:** Top Panel: Time variation of mean wave edge position for Regions A (solid) B (dashed) C (dash-dot) and D (dotted) as indicated in Fig 6.  Values are averaged at each column for 21 runs (solid line in Fig 12) and then averaged for all columns in the region. Bottom Panel: Time derivative of upper panel, corresponding to wave edge velocities.

# Optical Measurements of Tsunami Inundation and Debris Movement in a Large-Scale Wave Basin

M. Rueben, D. Cox*, R. Holman, S. Shin, J. Stanley

Oregon State University, Corvallis, Oregon 97331 USA

*corresponding author: dan.cox@oregonstate.edu

## Abstract

This paper presents optical measurements of debris movement and tsunami inundation over an unobstructed beach in a laboratory wave basin. The debris consisted of rectangular boxes and was placed unconstrained on a raised flat section of basin floor with no still water on the raised section. Debris movement was measured using two overhead video cameras and a novel object tracking algorithm. Two additional optical techniques, namely wave edge detection and particle image velocimetry (PIV), were used to compare optical and in-situ measurements of fluid velocity. The debris motion in the onshore direction was found to be repeatable while the offshore motion varied between trials. Debris tracking results from seven initial box configurations are discussed with respect to three factors: number of boxes, induced rotation, and segmentation of multiple-box groups. The results demonstrate the ability of the video data analysis to track multiple debris specimens and reliably measure their locations and orientations as a function of time. The data presented herein can serve as a benchmark for developing debris transport models.

## Keywords

Tsunami, laboratory experiments, debris, optical measurements, Argus, inundation, overland flow

## 1. Introduction

Recent tsunami disasters around the world have caused devastating loss of life followed by difficult recovery processes. The tsunami that struck Tohoku, Japan on March 11, 2011 originated from a magnitude 9.0 earthquake off the Japanese coast and resulted in over 15,000 deaths (Mori et al., 2011). Even tsunami barriers and reinforced concrete buildings were destroyed in what was considered an area well-prepared for a tsunami (Mori et al., 2011). Similar devastation was caused by other recent tsunamis, including the Sumatran tsunami in 2004 (Pomonis et al., 2006; Ruangrassamee et al., 2006; Saatcioglu et al., 2006), the Samoan tsunami in 2009 (Okal et al., 2010), and the Chilean tsunami in 2010 (Takahashi et al., 2010). Future tsunami events have the potential to cause similar damage. In the US Pacific Northwest, the Cascadia subduction zone (CSZ) has an estimated 14% chance of causing a 9.0 magnitude earthquake in the next 50 years (Groat, 2005). This event would likely trigger a 10 m high tsunami that would hit the coast in approximately 30 minutes (USGS 2006). The size and speed of such a tsunami stresses the importance of studying tsunami-related hazards to reduce fatalities and damage.

Takahashi et al. (2010) conducted a field survey after the Chilean earthquake and tsunami and found that several hundred shipping containers in the southern district of Talcahuano Port had been moved shoreward and had caused secondary damage to coastal structures via tsunami-debris impact. Takahashi et al. reported that approximately 30% of the shipping containers from Talcahuano Port had drifted out to sea and that sunken objects, including ships, hindered navigation and delayed the resumption of port activities. In rare cases, video footage has provided a glimpse of this kind of large-scale debris motion. Figure 1, for example, shows a succession of images from the Samoan tsunami in 2009 wherein multiple vehicles are pushed into a building by the initial inundation. Some recent

literature (e.g. Arikawa and Yashizaki, 2009; Arikawa et al., 2009; Matsutomi, 2009; Yeom et al., 2009) focused on debris impact and direct damage to structures. Although the tsunami-debris impact is an important issue, this paper focuses on the transport phase of debris motion, with no direct treatment of the impact itself. The overall aim of this paper is to develop a benchmark data set that can be used to guide the development of tsunami debris transport models by quantifying the motion of individual debris subjected to a transient wave.

It is noted that the work in this paper is part of a three-year study related to tsunami inundation forces and consisting of two-dimensional hydraulic tests in a large-scale flume in Year 1 (e.g., Oshnack et al., 2009; Oshnack et al., 2010) followed by three-dimensional hydraulic tests in a large-scale basin in Year 2 (e.g., Bridges et al., 2011; Thomas and Cox, 2012) as well as other work to develop design tools to resist tsunami forces (Park et al., 2010). Both experiments were conducted at the Network for Earthquake Engineering Simulation (NEES) Tsunami Facility located at Oregon State University and supported by the National Science Foundation. The Year 1 and Year 2 experiments were respectively termed 'Housesmash' and 'Housesmash2' to distinguish them from other tsunami studies conducted at the facility. As part of the NEES program, the data were made available to other researchers at the conclusion of the project (e.g., Baldock et al., 2009). Therefore, the instrument naming convention and coordinate system from the facility are adopted in this paper for consistency.

This paper presents novel applications of optical techniques to observe and measure fluid and debris motion for certain trials within the 'Housesmash2' experiment and is a continuation of earlier work by Rueben et al. (2010) that developed optical methods for tsunami inundation measurements in laboratory basins. This paper is outlined as follows.

Section 2 presents the large-scale, hydraulic model basin, instrumentation, and specimens

(debris models). Section 3 presents the trial procedures and rationale for the selection of

initial debris configurations. Section 4 presents two optical techniques for quantifying wave

motion: bore front tracking and free surface velocity estimation. Section 5 presents an

optical technique for measuring the position and orientation of each debris specimen.

Section 6 discusses the repeatability of the debris motion as demonstrated by the tracking

results. Section 7 examines the effects of three aspects of the initial configurations on debris

motion by comparing optical tracking results across different trials. Section 8 concludes this

paper by summarizing its main findings.

## 2. Facilities, Equipment, and Experiment

### 2.1 Wave Basin and Bathymetry

The 'Housesmash2' experiment was conducted in the Tsunami Wave Basin (TWB) at the

O.H. Hinsdale Wave Research Laboratory (HWRL), Oregon State University. An overview

photograph of the experimental setup is shown in Figure 2 and a detailed schematic in

Figure 3. The wavemaker specifications and wave basin bathymetry were identical to those

used for several other studies at the same facility (Cox et al., 2008; Baldock et al., 2009;

Swigler and Lynett, 2010; Rueben et al., 2010; Bridges et al., 2011; Thomas and Cox, 2012).

The description by Rueben et al. is adapted as follows for convenience. The basin was a

rectangular box, 48.8 m long by 26.5 m wide by 2.1 m high. The basin was equipped with a

segmented, piston-type wavemaker with a maximum stroke of 2.1 m and maximum velocity

of 2.0 m/s that was specifically designed to generate precise, long waves for tsunami

research. The coordinate system of the wave basin was defined as follows (see Figure 3).  X

was positive in the direction of wave propagation (to the west) with $X = 0$ at the neutral

position of the wavemaker. Y was positive to the south with $Y = 0$ along the centerline of the

basin. Z was positive up with $Z = 0$ on the basin floor. Beginning at the wavemaker, the

bathymetry was comprised of a constant depth section for $0 < X < 10$ m at $Z = 0$ m followed

by a 1:15 slope for $10 < X < 17.5$ m, followed by a 1:30 slope for $17.5 < X < 32.5$ m and

ending with a raised flat section for $32.5 < X < 43.75$ m at elevation $Z = 1$ m above the basin

floor (Figure 3, elevation view). The impermeable bathymetry was constructed of smooth

concrete with a float finish, and the roughness height was estimated to be 0.1 – 0.3 mm.

Starting at $X = 17.5$ m from the wavemaker, the basin was divided into three sections to

allow for three experiments to take place concurrently (see Figure 3, plan view). This layout

was identical to that described by Thomas and Cox (2012) and by Bridges et al. (2011), so

their descriptions are adapted as follows for the reader's convenience. The 'Cannon Beach'

project occupied the southernmost 4.75 m width of the tank while the Texas A&M

University project occupied the northernmost 7.8 m width. The 'Housesmash2' project was

conducted in an 8.4 m wide section in the center; data from two 'Housesmash2'

experiments, named 'Kinematics' and 'SlidingBox', are used for this paper.  The

'Housesmash2' area was centered in the field of view of two high-resolution cameras that

were part of the Argus observation network (Holman and Stanley, 2007; Rueben et al.,

2010).  The projects were separated by smooth plywood walls anchored to the floor with

metal brackets and sealed to eliminate the flow of water between the different projects.

Two narrow channels existed between the study sections and were used for instrument

amplifiers and to stage specimens for related studies.  In the back (west) end of the basin, a

thick layer of well-sorted crushed rock with nominal diameter of approximately 5 cm was

used to dampen the reflected wave energy and to decrease the time needed to quiet the

basin after each run. A rectilinear grid composed of 3 cm wide black lines with 0.6 m by 0.6

m spacing was painted onto the flat concrete section to accommodate the repeatable

placement of the debris specimens. The characteristic length scale of 0.6 m was used for the

debris specimens because this corresponded at approximately 1:20 scale to the standard 40

ft (12.2 m) long shipping containers that can typically be found in coastal waterfronts.

Debris specimens had square footprints for simplicity and to facilitate grouping of boxes

into larger square configurations as described in Section 3.2.

## 2.2 Instrumentation

The in-situ data for this project were recorded and stored using a National Instruments 64-

channel PXI-based real time data acquisition system with a sampling rate of 50 Hz and

duration of approximately 80 s.  The sampling rate was set at the maximum allowable rate

for the acoustic-Doppler velocimeters (ADVs, Nortec Vectrino). The sampling duration was

sufficient to capture the full inundation as well as much of the return flow, although the in-

situ velocity in the leading edge of the tsunami could not be measured by ADVs due to air

entrainment. All time values in this paper reference the data acquisition system and camera

images were synchronized to these values in post-processing.

Figure 3 shows the location of the in-situ instrumentation used for this study.  Eight wire

resistance wave gages and six ultrasonic wave gages (Senix Corporation TS-30S1-IV) were

mounted in the basin.   Of these, two ultrasonic wave gages (USWG3 and USWG4) were

located onshore for the 'SlidingBox' trials. For this work, these two gages were primarily

used for synchronizing the camera data with the in-situ data. For the 'Kinematics' trials used

in Section 4, USWG4 was co-located with an acoustic-Doppler velocimeter (ADV2) near the

centerline of the basin at X = 31.89 m, Y = 0.54 m.

Optical instrumentation for this work was identical to that used by Rueben et al. (2010).

Two Argus cameras were located directly over the basin at tank coordinates X = 39.98 m, Y

= -0.96 m and X = 32.41 m, Y = 10.78 m. The Argus cameras were Scorpion FireWire imagers

featuring 1280x960 pixel, 8-bit, Bayer-encoded CCD sensor chips and 4.5 mm lenses

spanning a 69° horizontal field of view. The spatial resolution and long-term stability of

these same cameras are reported by Rueben et al. (2010, Section 3). Frame rate was set to 5

Hz for 'Kinematics' trials and 2 Hz for 'SlidingBox' trials. Each pair of collected frames from

the two cameras was synchronized and projected to a rectified plan view at a single

elevation (Z-value), and then merged into a single image (e.g., Rueben et al., 2010).

Rectifying and merging camera frames was automated by tools included in the Argus

Database as used by Rueben et al. (2010) and described by Holman and Stanley (2007).  An

example pair of images merged to Z = 1 m is shown in Figure 3 to depict the overall field of

view.

**2.3 Debris Specimens for Optical Tracking**

The debris specimens were constructed from one half inch (12.7 mm) thick plywood. Each

box had a nominal footprint of 60 cm x 60 cm and was nominally 40 cm tall. The sides of

each box were painted gray with a black number on one side for unique identification from

a distance and a black scale to facilitate run-up observations via webcam. Nominal dry

weights were 14.5 kg (±1 kg) per box without pavers. One box, designated with a black lid,

was loaded with three pavers and remained stationary throughout each trial so as to act as

an obstacle for other debris. This box will be referred to as the "stationary box" for the

remainder of this paper. The remaining boxes contained no pavers and were allowed to

slide or float with each wave. These will be called "sliding boxes." The lids of the sliding

boxes were painted to facilitate video image tracking: two yellow circles (15 cm and 20 cm in diameter) for tracking orientation and up to six orange circles (10 cm in diameter) for identifying the box number from above, all on a blue background for contrast. Unique box numbers were used to demonstrate a method for tracking individual boxes. All paints were low-gloss to prevent reflections of the ceiling lights from reducing the contrast between colors in the images. Figure 2 shows an example configuration of boxes (Config 8; see Section 3.2 for box configurations) on the shore section of the TWB floor. The direction of wave propagation is indicated by a green arrow for reference, and this was also the positive X-direction in the TWB coordinate system (see Figure 3).

## 3. Test Program

### 3.1 Experimental Process

The experimental procedure was similar to that used for previous 'Housesmash2' trials, so this section includes descriptions adapted from Thomas and Cox (2012) and from Bridges et al. (2011) for convenience. The experiment was conducted with a water depth of 90.56 cm with a standard deviation of 0.13 cm based on measurements before each trial.  With this water level, the still water shore line was located at X = 29.8 m and approximately 3 m from the start of the flat inundation section at X = -3.0 m (see Figure 3). All of the waves broke seaward of this position and advanced over the flat section as a broken bore.  An error function was used to generate the paddle displacement so that the full 2 m stroke of the wavemaker could be used, even for relatively small tsunami heights of 10 cm or less, thereby maximizing the duration of the inundation process.  Conventional solitary wave generation techniques (e.g., Goring, 1978) would have limited the inundation for the smaller

wave heights.  Only one wave type, denoted "ERF = 7 s", was generated for the specific trials

chosen for this paper.  For this wave type, the wavemaker paddles were actuated according

to an error function with a 7 s period and 4 m displacement. Figure 4 shows example in-situ

data from 'Kinematics' Trial 15. Figure 4a shows the wavemaker displacement time series

generated using the 7 s error function utilizing the full stroke 2 m of the wavemaker while

retaining a small amplitude wave of approximately 10 cm height.  The free surface time

series is fairly symmetrical leaving the waveboard (Figure 4a) and continues to have a fairly

symmetrical shape and constant height as it propagates over the flat section of the basin

(Figure 4b) for 20 < t < 30 s.  The free surface becomes asymmetric and increases in height

as the wave propagates over the slope (Figure 4b, WG6), breaks, and propagates over the

flat, raised portion of the basin as a broken bore (Figure 4c).  The bore velocity (Figure 4d)

is highest at the leading edge, and the ADVs had difficulty capturing the velocity in the

leading edge due to air entrainment as will be discussed in Section 4.

The entire run sequence – wave generation, propagation, and inundation – had a duration of

about 2 minutes. Subsequently, data were uploaded to the NEES Experiment Notebook and

all data channels were inspected visually before the start of the next run.  Any remaining

water was removed from the flat section of the beach using squeegees, specimens were

positioned according to the next configuration, and the basin was allowed to calm before

the start of the next trial.

## 3.2 Debris Specimen Configurations

Each of the 'SlidingBox' trials began with the debris specimens ("boxes") arranged in a

predetermined initial configuration (e.g. "Config 5"). After wave generation, the bore

propagated over the raised section and moved the boxes onshore.  The stationary box, when

used, remained as a fixed obstacle. Table 1 shows the seven unique configurations chosen

for this study. Each configuration was tested only once due to time constraints except Config

4, which was used for six trials to verify repeatability (discussed in Section 6).

The seven configurations were designed such that three aspects of initial debris

configurations could be studied: the number of boxes, induced rotation, and segmentation

of groups (discussed in Section 7). For Configs 1, 3, 7 (first column of Table 1), the box

motion was primarily translation with little rotation. The number of boxes was increased

from 1 to 4 to 9, respectively, while maintaining a square pattern.  For Configs 2, 4, 8

(second column of Table 1), the setup was identical to Configs 1, 3, 7, except that a fixed box

was added to induce rotation.  Config 12 (third column of Table 1) was added with four

boxes joined together to compare the motion with the four individual boxes in Config 4.

Section 7 discusses detailed comparisons of debris motion for the different configurations.


## 4. Bore and Surface Tracking

The bore motion over the raised section was studied prior to introducing the box specimens

described in the previous section. Bore motion was analyzed using two optical techniques

on five 'Kinematics' trials with wave type ERF = 7 s. Video frames were projected to shore

level (Z = 1 m) when measuring wave motion. The bore edge position was calculated on a

frame-by-frame basis using an algorithm similar to that described by Rueben et al. (2010).

Useful corollaries of the bore edge position include the time of debris contact and the

average bore velocity at a desired time or location. In addition, the free surface velocity of

the inundation was estimated by tracking the movement of surface foam. This analysis was

carried out using the MPIV (MATLAB Particle Image Velocimetry) toolbox, which tracks the

motion of persistent shapes across successive video frames.  Use of MPIV was limited to the

specific times and locations in which high-contrast foam was visible. Figure 5 shows the average results of both the edge tracking and the surface velocities for 5 frames, each 1.0 s apart, during the initial inundation for 'Kinematics' Trials 15, 28, 32, 37, and 42. The leading edge is shown as a dashed line with +/- one standard deviation calculated from the edge detection algorithm, and the surface velocities are shown as velocity vectors, with the vector scale of 3 m/s shown near the top of Figure 5e. Figure 5a shows the broken bore at X = 31 m just prior to the inundation over the raised section starting at X = 32.5 m. Figures 5b, 5c, and 5d show the inundation past the initial starting position of the debris to be placed at X = 34.5 and that the velocity is uniform across the basin width in the absence of debris. Figure 5e shows the inundation well past the initial debris positions.  Here, the leading bore edge becomes less uniform across the basin width, and the loss of persistent foam decreases the number of velocity vectors resolved by the MPIV.

Figure 6 shows how the optical and in-situ measurements were combined to compensate for the inability of the ADVs to capture the leading part of the flow due to air entrainment and the inability of the optical method to capture the surface velocity later in the flow due to a lack of persistent foam.  The measurements were taken for 'Kinematics' Trial 15 with in-situ measurements taken from co-located USWG4 and ADV2 at X = 31.89 m, Y = 0.54 m. Figure 6a shows the free surface of the bore in the range 32 < T < 38 s and that the signal is well-resolved by the USWG despite the presence of air entrainment.  The leading edge arrives at T = 32.8 s and reaches a maximum approximately 3 s later. Figure 6b shows the combined in-situ and optical velocity measurements over the same time.  The in-situ velocity (dots) can be resolved after the leading part of the flow has passed (T > 33.6 s), but completely misses the leading edge velocity (32.8 < T < 33.6).  The vertical lines show the optical measurements of the surface velocity using the MPIV routine.  They agree well with the in-situ measurements and provide velocity information earlier than the ADV does, but

not at the leading edge. The velocity can be resolved at the leading edge by the edge tracking routine and is shown by the star symbol. Combining these three velocimetry techniques allows for a line of best fit (black line, Figure 6b) that represents a reasonable estimation of the fluid velocity for the entire time period of interest. Figure 6c shows the momentum flux estimated as the product of the free surface times the square of the velocity. Although we do not use the momentum flux elsewhere in this paper, it may be a useful quantity for predicting the initiation of debris movement. Figure 6c shows that the peak momentum flux occurs approximately 0.3 s after bore arrival and 2.7 s before the maximum height.

## 5. Debris Tracking Methodology

An image processing technique was developed for measuring the position and orientation of multiple debris specimens using a unique paint scheme for the box lids. Video frames were projected to box lid level (Z = 1.4 m) when measuring box motion. The HSV (hue, saturation, value) color map was used to analyze the images instead of the more familiar RGB (red, green, blue) system. Hue is a pixel's color, saturation is the amount of color, and value is the brightness. The yellow, orange, and blue colors for the box lids were chosen such that they could be differentiated in all three channels, thereby increasing object tracking certainty. Figure 7 shows an example of the box tracking process. Figure 7a shows the original image. The first step in the box tracking algorithm is to identify the blue background on the box lid using handpicked thresholds. The outline of the blue background is used as a mask to isolate the box lid for further processing by eliminating the rest of the image. The yellow dots are identified next within the isolated box lid image (Figure 7c). By counting the pixels in each dot, the algorithm can distinguish between the two different dot

sizes and check to make sure each dot is of the expected size (i.e. that the entire yellow

circle has been selected). The yellow dots define the box position and orientation within the

Tsunami Wave Basin's local coordinate system. These data are then used to infer the

expected locations of the six orange dots that indicate the box number. Checking for each

orange dot at its expected location yields the box number via a binary numbering system

invented for this experiment. This completes the box tracking algorithm, as all four aspects

of the box state have been determined: box number, X-position, Y-position, and orientation

angle (Figure 7d). The successful calculation of these data is verified by the green box

outline in Figures 8 and 9.  Figures 8-14 show sample merged video frames overlaid with

tracking results for all seven initial configurations chosen for this study.  Figure 15

summarizes the initial debris motion in configurations with rotation induced by a stationary

box (Configs 2, 4, 8, 12), as will be examined in Section 7.2.


## 6. Repeatability of Debris Motion

Config 4 was used for all of the six trials that provided the data for the repeatability analysis

in this section.  It is assumed here by necessity that repeatability findings for Config 4 are

applicable to all configurations.

Debris position repeatability was studied first by comparing box paths over the six trials

that used Config 4.  The centroid (average) box paths for all six trials are plotted together in

Figure 16a, which shows repeatable onshore motion (see Figure 16b) followed by divergent

offshore motion.  More specifically, the onshore motion became less repeatable as the box

slowed to a stop and the offshore motion diverged into two separate trends in the +Y and –Y

directions.  The variation between trials was larger during the offshore motion.  Box 2 was

chosen for individual study in Figure 17 because the offshore paths (Figure 17a) all curved

in the +Y direction (Cf. Figure 9), unlike the other individual boxes. The repeatability trend was similar, although the standard error in the Y direction increased more sharply near the end of the onshore motion for Box 2 (Figure 17b) than for the centroid (Figure 16b).

Thus far, it has been useful to divide box motion into the highly repeatable onshore motion and the more variable offshore motion. This division defines three key waypoints for each box: first, the "start point" or initial configuration, then the "stall point" where the cross-shore (X) velocity is zero and cross-shore motion transitions from onshore to offshore, and lastly the "stop point" where the box settles by the end of the trial. Figure 18a plots the stall points for each box over all six trials, and Figure 18b does the same for the stop points. Stall points were well-grouped, always within a 2 m square and even, for Boxes 1 and 3 (right-hand column), within a 1 m square. Stop points were more scattered. Some, like for Box 1, were at least on the same side (-Y) of the initial configuration, while others, like for Box 3, were on both sides. The general trends from Figure 18 agree with the conclusions from Figures 16 and 17: stall points were closely-packed due to the repeatability of the onshore motion, while the stop points were much more scattered even for each individual box.

Repeatability of box motion for Config 4 was also assessed for box velocities. Figure 19 shows individual box velocities in the cross-shore (X) direction over all six trials. Note that these velocities can be roughly compared with the Box 2 paths in Figure 17 by estimating the space between consecutive box positions (black dots), which occur at 0.5 s intervals. Also note that the debris velocity crosses zero at stall and stop points by definition, enabling comparison with Figure 18. Velocities, like positions, were more repeatable during the onshore motion than during the offshore motion. More notably, the onshore velocities for the right-hand column (Boxes 2 and 4) were less repeatable than for the left-hand column (Boxes 1 and 3), especially near the stall point. The offshore velocity was not very

repeatable for individual boxes but tended to vary between 0 and -1 m/s.  Peak onshore

velocities were similar and ranged from 1 to 1.5 m/s.  Repeatability was also assessed for

the centroid velocity as shown in Figure 20. This plot can also be compared with Figure 16

by observing the space between box positions.  Onshore centroid velocities, like the

individual box velocities, were generally repeatable. The offshore centroid velocities in

Figure 20 appear relatively repeatable, but the individual box velocities demonstrate

otherwise; proceed with caution when constructing general trends from offshore centroid

velocities as in Figures 21b.  Overall, this repeatability analysis lends credence to the

onshore motion results presented in Section 7 while providing a clear depiction of how

offshore motion varies for different trials and boxes.

## 7. Effects of Initial Configuration on Debris Motion

This section presents the debris motion results with special focus on three aspects of the

initial configurations (Table 1).  Section 7.1 studies the effects of the number of sliding

boxes on motion (left column of Table 1).  Section 7.2 studies the effects of induced rotation

by the stationary box on the sliding boxes (middle and right columns of Table 1).  Section

7.3 studies the effects of segmentation, or the breaking apart of initial configurations that

contain multiple sliding boxes (middle and bottom rows of Table 1).  These three categories

were chosen for their relevance to real-world tsunami debris and because the initial

configurations for this experiment were well-suited for their study.  All initial

configurations presented in the following subsections were only tested once, with the

exception of Config 4. The data from all chosen trials are assumed, however, to be

repeatable based on the analysis in the previous section.

**7.1 Number of Sliding Boxes**

Figure 21 shows the effect of the number of boxes in the initial configuration on the cross-shore debris velocities. Configs 1, 3, and 7 were chosen for Figure 21 because they each have a square configuration with a different number of sliding boxes. None of the boxes were connected to each other in any of these three configurations, so the breakup (segmentation) of the initial configuration remains relevant to this discussion. For Configs 3 and 7, cross-shore velocities were averaged for each time step, which is equivalent to calculating the centroid velocity. The variation in velocity between the boxes was represented as a standard error for those configurations; the 95% confidence intervals are shown on Figure 21b as error bars. The errors were reasonably low, especially before the peak velocity at around T = 38 s. After peak velocity, the boxes were often slowed by the reflected wave, which also caused them to float. Section 6 observes that floating debris motion is less repeatable than sliding debris motion, hence the increased uncertainty values in regions such as T = 45 – 50 s. The acceleration period prior to T = 38 s shows that increasing the number of boxes slowed acceleration and both lowered and delayed the peak velocity. The lower accelerations could have resulted from a locally slower bore due to the wider frontal areas, while the lower peak velocities were most likely due to the reflected wave contacting the boxes before they had much time to gain speed. Figures 22 and 23 show similar trends. The initial configurations chosen for Figure 22 (Configs 2, 4, 8) were the same as those chosen for Figure 21 with the addition of a stationary box to induce rotation. Figure 22 shows that the peak velocities decreased with the addition of more boxes, but the peak velocity delay between Configs 4 and 8 is not so clearly evident, perhaps because of the unusual behavior of the rightmost column of Config 8 (see Figure 14). Decreased peak velocity and peak velocity delay are both apparent, however, between Configs 2 and 12 in Figure 23.

**7.2 Induced Rotation**

Figure 15 shows the initial debris motion in configurations with induced rotation. Figures 8 and 9 are useful for studying the effect of induced rotation on a single-box configuration. Figure 8 shows Config 1, the configuration without rotation. The box slid across the basin floor in a linear cross-shore path before reaching the back of the wave basin. The reflected wave, clearly visible around X = 41 m in Figure 8d, then propelled the box back toward the wavemaker. By this time, the water depth around the box was sufficient to cause floating, which greatly reduced trial repeatability as observed in Section 6. Figure 9 shows a single sliding box forced to rotate by a stationary black box placed at its bottom-right corner. This caused a counter-clockwise rotation that continued throughout the sliding box's motion. The path of the sliding box was also shifted by over 60 cm in the -Y direction relative to the path for Config 1 (see Figure 8). The wave energy imparted on the sliding box was divided between linear and rotational kinetic energy for Config 2, while all imparted wave energy in Config 1 was linear. Comparing Figures 9 and 12 reveals that adding more boxes as in Config 12 yielded a similar debris path as for a single box, although rotation was reduced and the cross-shore motion reversed nearer to the initial position. Both of these differences from the single-box Config 2 (Figure 9) are consistent with the effects of adding more boxes observed in Section 7.1. Figure 23 compares velocity profiles for Configs 1, 2, and 12. It is interesting that the peak velocities for Configs 1 and 2 were so similar despite the onshore velocity profile being slightly delayed for Config 2 (note sides of profile). Figure 23 also agrees with our analysis of Config 12: the slowed debris acceleration resulted in a lower peak velocity and the reflected wave traveled farther offshore before impacting the debris, so the motion reversed later than for Configs 1 and 2 by about one second. Although Figure 23 also seems to indicate that configurations with induced rotation had faster offshore motion, the discussion of Figure 19 in Section 6 warns that offshore motion was not very

repeatable.  Additional repetitions of these configurations would be necessary to investigate this possibility.

**7.3 Segmentation of Debris Groups**

Configs 3, 4, 7, and 8 studied the potential for groups of debris specimens to segment and disperse.  A common trend for all four of these configurations was the tendency to first break into cross-shore oriented columns and then into individual boxes.  Figures 10 and 13 show the simplest examples, Configs 3 and 7.  The columns split off symmetrically such that the centroid path was almost perfectly straight in the onshore (+X) direction.  It is interesting to note that the centroid paths for these two configurations are shown in Figure 21a to be very similar to that of Config 1.  Figure 11 captures similar columnar behavior for Config 4.  As can be seen from the video frames, the southern column (right side in Figure 11) was prevented from moving in the onshore (+X) direction by the stationary box (Figure 11a) and rotated as a unit (Figure 11b) before breaking apart and sliding shoreward (Figure 11cd).  The northern column (left side) sheared away in nearly pure translation (Figure 11a).  Its slight rotation (Figure 11b) was caused by interaction with the southern column. The debris group was completely segmented by the time the boxes reached their maximum shoreward positions (Figure 11d).  The most complex case was that of Config 8 (Figure 14), in which the two northern (left) columns blocked the southern (right) column's rotation such that it rotated in the opposite (clockwise) direction and stopped, ostensibly finding an equilibrium angle.  All this debris motion, both simple and complex, was captured by the Argus cameras both for synoptic review via video and for quantification via the box tracking algorithm.

The effects of segmentation were made especially apparent by Config 12. Figures 11 and 12 directly compare Configs 4 and 12 by calculating the centroid motion of the boxes for both tests. The centroid for any configuration is defined as the average of all the box center locations. Figures 11 and 12 show the path of the centroid plotted in green, and the green star shows the convergence of the box center locations to form the current centroid location. The centroid path for Config 4 was more linear than for Config 12 (Figures 11e, 12e), but at a diagonal, whereas for contiguous debris as in Configs 2 and 12 the stationary box caused tight rotation followed by spinning translation in the +X direction. Figure 24b presents velocity data for Configs 4 and 12. The onshore velocity profile for Config 4 was shorter and wider than for Configs 3 and 12; accelerations and the peak velocity were both slow. This is difficult to interpret for two reasons. First, it has already been noted that the boxes in Config 4 split into two columns with very different behavior, hence the large standard error bars in Figure 24b. Second, Config 4 differed from Config 3 in that it had induced rotation and from Config 12 in that it allowed for segmentation, so the cause of the slower acceleration is unclear. One possible conclusion is that more pronounced segmentation causes a wider velocity profile. Config 12 had no segmentation and the narrowest profile, Config 3 underwent a prolonged segmentation process and had a slightly wider profile, and Config 4 segmented quickly and in a complex manner, which may explain its wide, shallow velocity profile.

## 8. Conclusion

This paper presents an analysis using optical techniques of tsunami-debris movement during laboratory experiments performed in a large-scale wave basin. Trials were run with up to nine mobile debris specimens on an elevated section fronted by an alongshore

uniform slope. Specimens were placed in seven different initial configurations, some with an additional, fixed specimen to induce rotation. One initial configuration was tested six times to study the repeatability of the debris motion. Configurations were designed to study debris translation and rotation as well as the effects of debris quantity and segmentation of groups. Most of the data for this paper were collected by two overhead cameras, and optical tracking results from these cameras summarize both the wave and debris motion. In-situ instruments such as ultrasonic wave gages were used for timing and to estimate momentum flux in combination with the tracking results.

Based on this work, the following conclusions can be made:

1. Optical and in situ measurements are consistent such that combining them is useful. For example, optical measurements were used to compensate for instrument limitations and provide a full time series of estimated momentum flux (Figure 6).

2. The optical debris tracking technique reliably tracks as many as nine boxes. Tracking results are accurate and can be plotted over camera images to provide insight into motion trends (e.g. Figure 14).

3. Debris motion is very repeatable during the onshore motion but much less repeatable during the offshore motion, during which the boxes are floating instead of sliding. This is true of both debris positions (e.g. Figure 18) and velocities (e.g. Figure 19). Regarding positions, this may allow for prediction of which buildings an object might strike, but not of where that object might settle. Debris impact velocities may also be predictable, but only during the onshore motion.

4. Increasing the quantity of debris specimens both lowers and delays the peak average velocity (Section 7.1). This may be due to the bore front being slowed by the larger frontal area and mass of the multiple-box group.

5. Fixed obstacles rotate the debris and divert it from a linear onshore path, but the peak average velocity is not significantly affected (Section 7.2).

6. Groups of debris tend to split into columns parallel to the direction of fluid flow (Section 7.3). These columns travel symmetrically until broken up by disturbances like a reflected wave or obstacle.

The increased understanding of debris motion from just these trials is impressive and constitutes grounds for the continued use of optical measurement techniques in tsunami-related laboratory experiments.

## Acknowledgements

## References

Arikawa, T. and Yashizaki, M. (2009) "Large Scale Tests on Concrete Wall Destruction by Tsunami with Driftwood," *Proc. Conference on Coastal Engineering*, Japan Society of Civil Engineering, (in Japanese).

Arikawa, T., Ohtsubo, D., Nakano, F., Shimosako, K., Ishikawa, N. (2009) "Large Model Tests of Drifting Container Impact Force due to Surge Front Tsunami," *Proc. Conference on Coastal Engineering*, Japan Society of Civil Engineering, (in Japanese).

Baldock, T.E., Cox, D. Maddux, T., Killian, J., Fayler, L. (2009) "Kinematics of breaking tsunami wavefronts: A data set from large scale laboratory experiments," *Coastal Engineering*, 56, 506-516.

Bridges K., Cox, D., Thomas, S., Shin, S., and Rueben, M. (2010) "Influence of macro-roughness on tsunami runup and forces: Large scale experiments at the NEES Tsunami Facility," *Coastal Engineering*, Submitted 12/2010.

Cox, D., Tomita, T., Lynett, P., and Holman, R. A. (2008). "Tsunami inundation with macro-roughness in the constructed environment." *Proc. 31st Int. Conf. on Coastal Engineering*, ASCE, New York, 1421–1432.

Goring, D.G. (1978). "Tsunamis – the propagation of long waves onto a shelf," REP Kh-R-38, W.M. Keck Lab. of Hyd. and Water Resources, Calif. Inst. Technology., California.

Groat, C. G. (2005). "Statement of C. G. Groat, Director, U.S. Geological Survey, U.S. Dept. of the Interior." Statement before the Committee of Science, January 26, U.S. House of Representatives, Washington, DC.

Holman, R. A., and J. Stanley (2007) "The history and technical capabilities of Argus," *Coastal Engineering*, 54, 477-491.

Matsutomi, H. (2009). "Method for Estimating Collision Force of Driftwood Accompanying Tsunami Inundation Flow." *Journal of Disaster Research,* Vol. 4, No. 6, 435-440.

Mori, N., T. Takahashi, T. Yasuda, and H. Yanagisawa (2011). "Survey of 2011 Tohoku earthquake tsunami inundation and run-up." *Geophys. Res. Lett.*, 38, L00G14.

Okal, Emile A., Fritz, Hermann M., Synolakis, Costas E., Borrero, Jose C., Weiss, Robert, Lynett, Patrick J., Titov, Vasily V., Foteinis, Spyros, Jaffe, Bruce E., Liu, Philip L.-F., and Chan, I-chi (2010). "Field Survey of the Samoa Tsunami of 29 September 2009." *Seismological Research Letters*, Vol. 81, No. 4, July/August 2010, 577-591.

Oshnack, M.B., Aguiniga, F., Cox, D., Gupta, R., van de Lindt, J. (2009). "Effectiveness of Small Onshore Seawalls in Reducing Forces Induced by Tsunami Bore: Large Scale Experimental Study." *Journal of Disaster Research*, Vol.4 No.6, 382-390.

Oshnack, M.B., Shin, S., Cox, D., Galan, F., Knight, A. (2010). "Cross-Shore Variation of Tsunami Loads on Vertical Walls: Transition from Impulse Loads to Quasi-Steady Bores." *Journal of Waterway, Port, and Coastal Engineering,* (in review).

Park, S., van de Lindt, J.W., Cox, D., Gupta, R., Aguiniga, F. (2010). "Methodology for Development of Tsunami Fragilities," ASCE, *Journal of Structural Engineering*, (in review).

Pomonis et al. (2006). "The Indian Ocean Tsunami of 26 December 2004: Mission Findings in Sri Lanka and Thailand." United Kingdom: Institution of Structural Engineers.

Ruangrassamee, A., Yanagisawa, H., Foytong, P., Lukkunaprasit, P., Koshimura, S., and Imamura, F. (2006). "Investigation of tsunami-induced damage and fragility of buildings in Thailand after the December 2004 Indian Ocean tsunami." *Earthquake Spectra*, 22(S3), S377–S401.

Saatcioglu et al. (2006). "Performance of Structures in Thailand During the December 2004 Great Sumatra Earthquake and Indian Ocean Tsunami." *Earthquake Spectra*, 22, S355-S375.

Swigler, D. and Lynett, P. (2010). "Laboratory Study of the Three-Dimensional Turbulence and Kinematic Properties Associated with a Solitary Wave Traveling Over an Alongshore-Variable, Shallow Shelf." in review.

Takahashi, S., Sugano, T., Tomita, T., Arikawa, T., Tatsumi, D., Kashima, H., Murata, S., Matsuoka, Y., Nakamura, T. (2010). "Summary Report on Joint Survey for 2010 Chilean Earthquake and Tsunami Disaster in Ports and Coasts." *Technical Report of the Port and Airport Research Institute*, Kuriyama, Japan.

Thomas, S. and Cox, D. (2010) "Influence of Finite-Length Seawalls for Tsunami Loading on Coastal Structures." *Journal of Waterway, Port, and Coastal Engineering*, 138, 203-214.

USGS Tsunami Pilot Study Working Group. (2006). "Seaside, Oregon tsunami pilot study— Modernization of FEMA flood hazard maps." *Open-File Rep. 2006-1234*, U.S. Dept. of the Interior, U.S. Geological Survey, Washington, DC.

Yeom, G., Nakamura, T., and Mizutani, N. (2009). "Collision Analysis of Container Drifted by Runup Tsunami Using Drift Collision Model." *Journal of Disaster Research,* Vol 4. No. 6, 441-449.

**Figure 1:** Still frames from a security camera showing debris transport on the island of American Samoa during the September 29, 2009 tsunami. Vehicles in the parking lot are pushed into the structure at bottom left, causing damage. [Source: http://www.fbi.gov/honolulu/press-releases/2009/hn100909.htm]
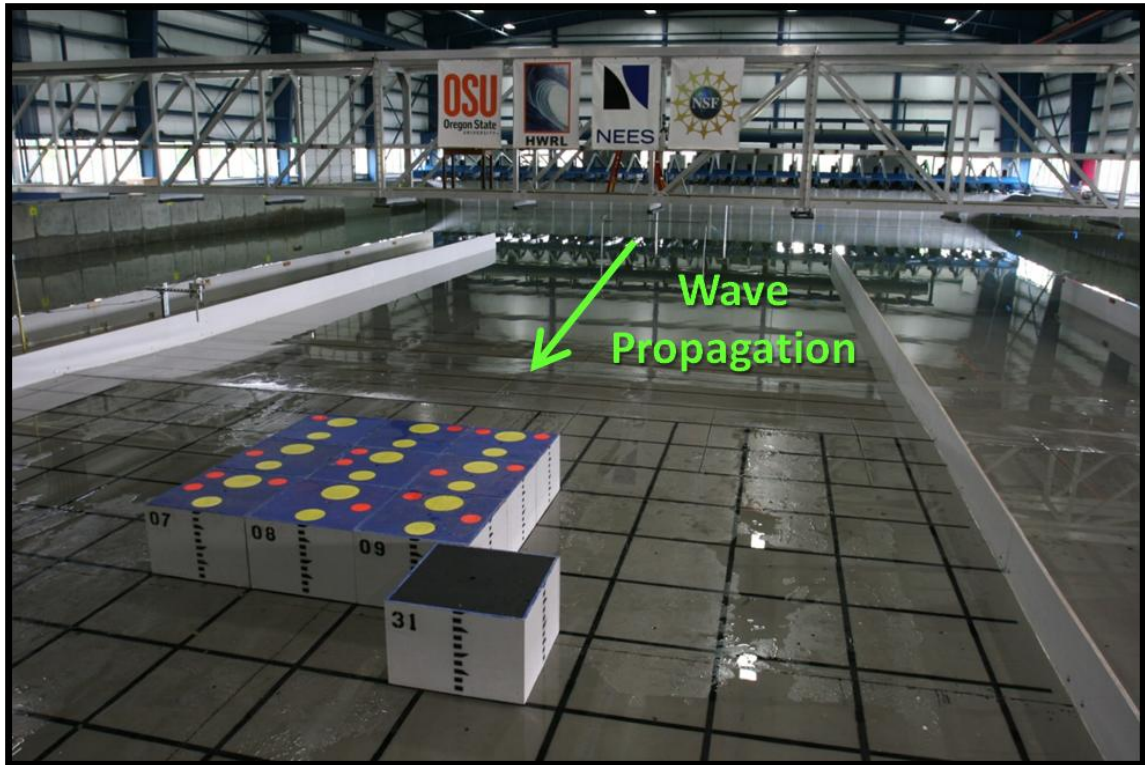
**Figure 2:** Config 8 awaiting a wave on the shore section of the TWB floor. Black gridlines form 60cm squares and white plywood walls divide NEEShousesmash2 tests from two other concurrent experiments. Green arrow indicates direction of wave propagation (positive X-direction in TWB coordinate system).
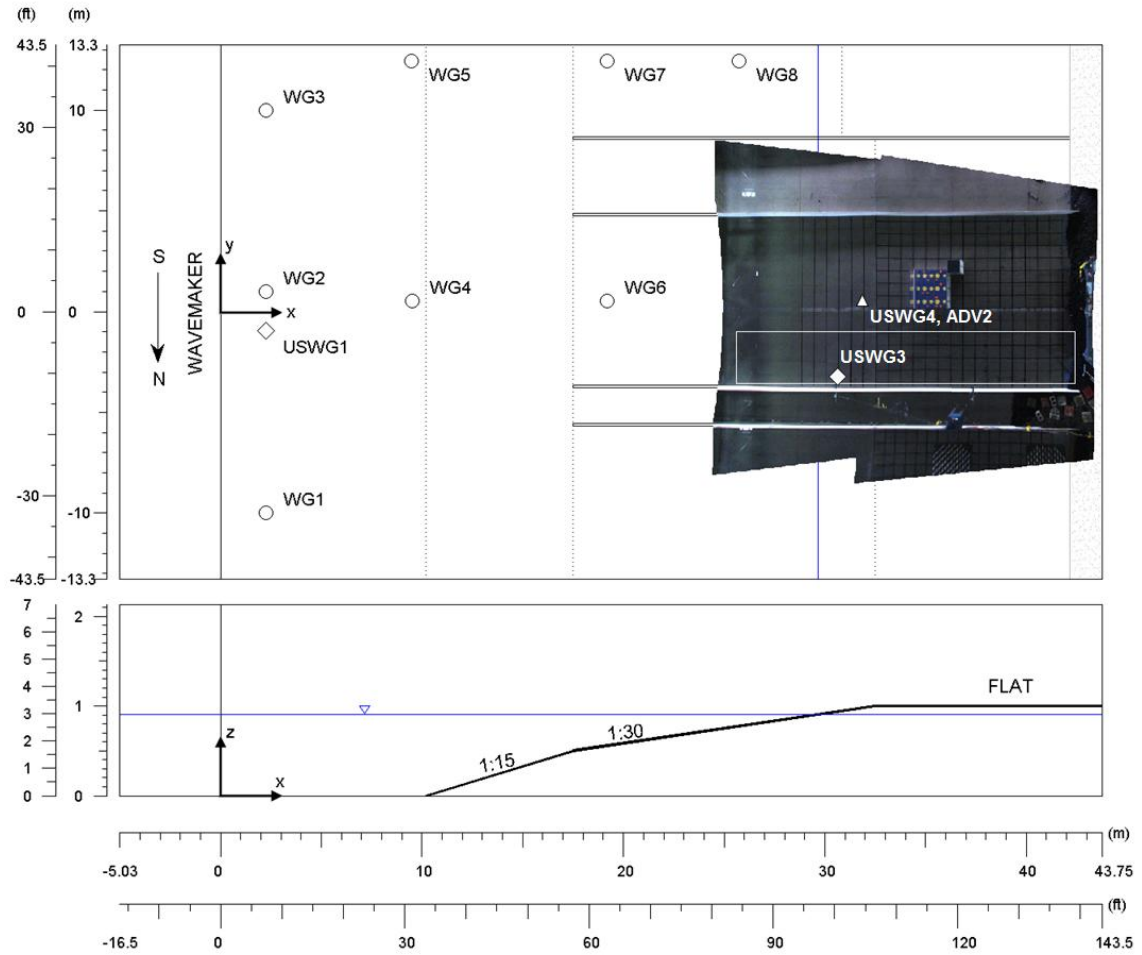
**Figure 3:** Schematic of the Tsunami Wave Basin (TWB) as equipped and instrumented for 'Kinematics' Trial 15. Plan view (top) includes locations of wire resistance wave gages (circles), ultrasonic wave gages (diamonds), and a USWG-ADV pair (triangle). Merged view from both overhead Argus cameras is displayed on the plan view. Elevation view (bottom) shows alongshore-uniform bathymetry and mean water level.
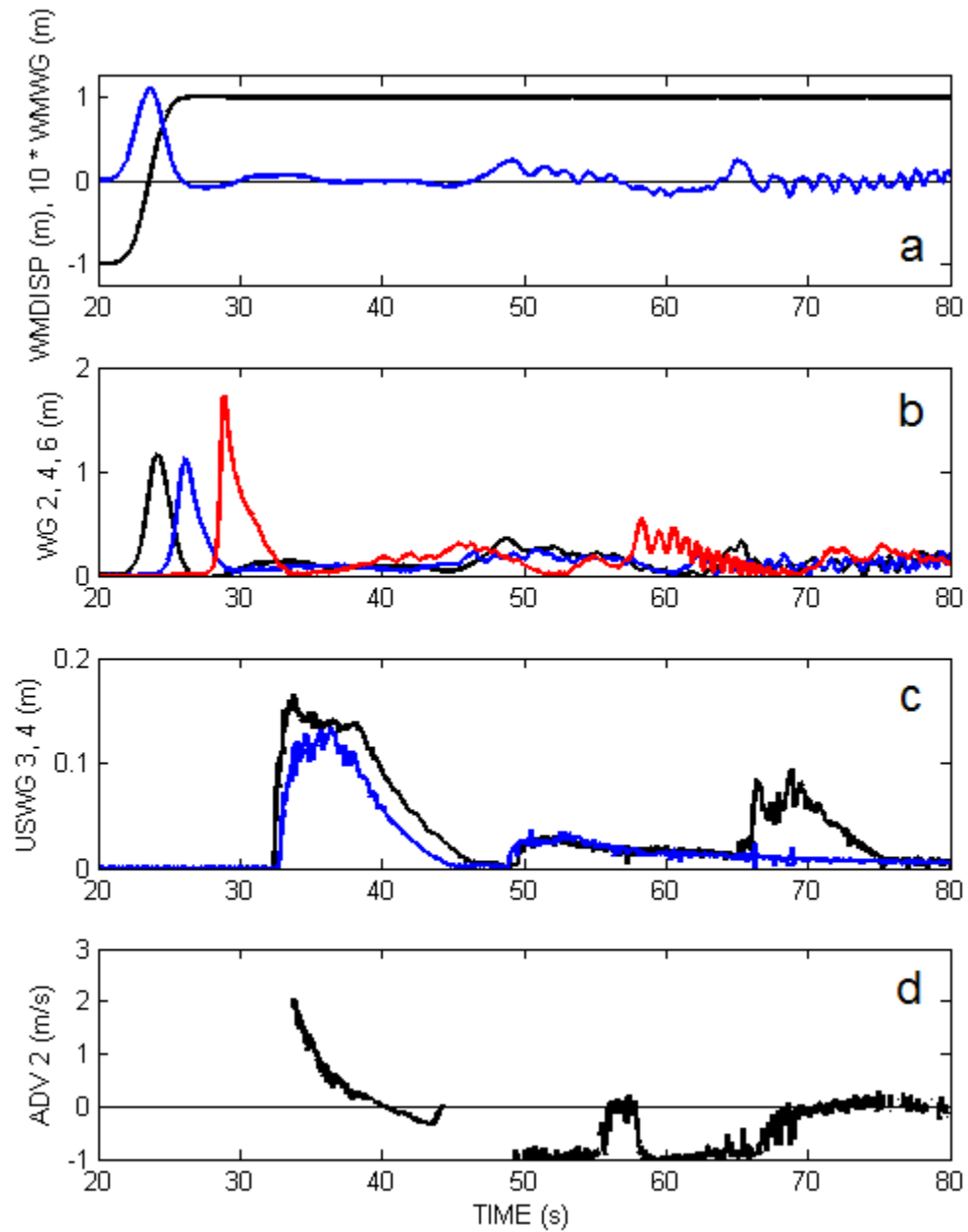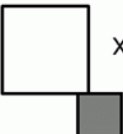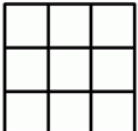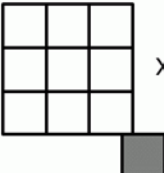
**Figure 4:** Example wavemaker and in-situ time series data from 'Kinematics' Trial 15. (a) Wavemaker displacement (black) and ten times wave height at wavemaker paddle (blue). (b) Wave height at WG 2 (black), WG 4 (blue), and WG 6 (red). (c) Bore height at USWG 3 (black) and USWG 4 (blue). (d) Cross-shore fluid velocity at ADV 2.

| No. of Boxes | Free, Transl. | Free, Transl. & Rot. | Joined Transl. & Rot. |
|---|---|---|---|
| 1 | **Config 1** ☐ x1 | **Config 2** ☐ x1 | |
| 4 | **Config 3** ⊞ x1 | **Config 4** ⊞ x6 | **Config 12** ☐ x1 |
| 9 | **Config 7** ⊞ x1 | **Config 8** ⊞ x1 | |

Wave Propagation ↓

**Table 1:** Simplified diagrams of the seven unique initial box configurations discussed in this paper. White "sliding" boxes are free to move along the floor; gray "stationary" box is fixed. Repetitions are also displayed, e.g. "x6" indicates six repetitions of the same configuration.
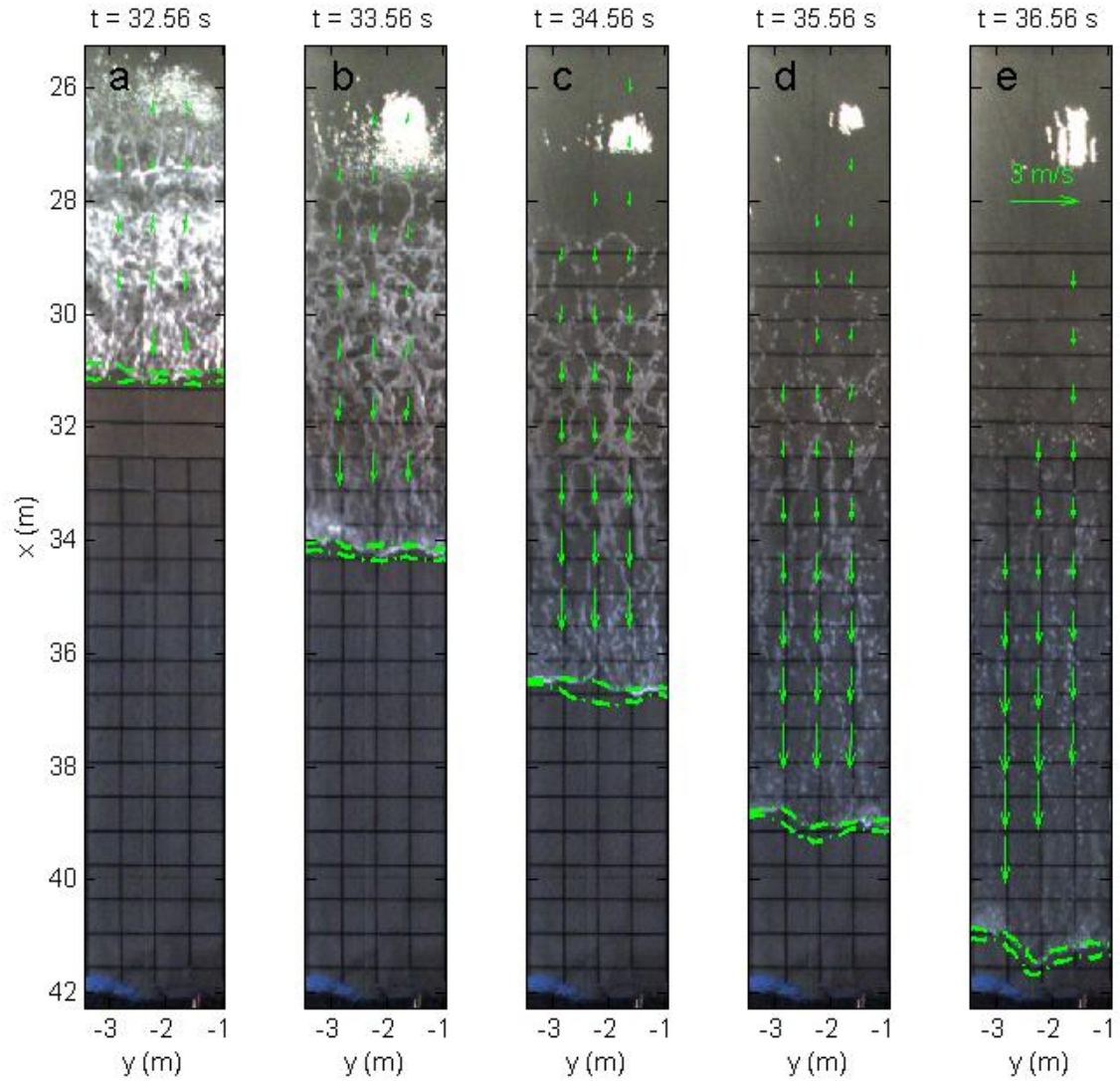
**Figure 5:** Bore and surface tracking results from 'Kinematics' Trials 15, 28, 32, 37, and 42 shown over merged images from 'Kinematics' Trial 28. Wave type for these trials is ERF = 7 s. Arrows indicate surface velocity estimations from MPIV analysis. Dashed lines show +/- one standard deviation from mean wave edge position as calculated by edge detection analysis.
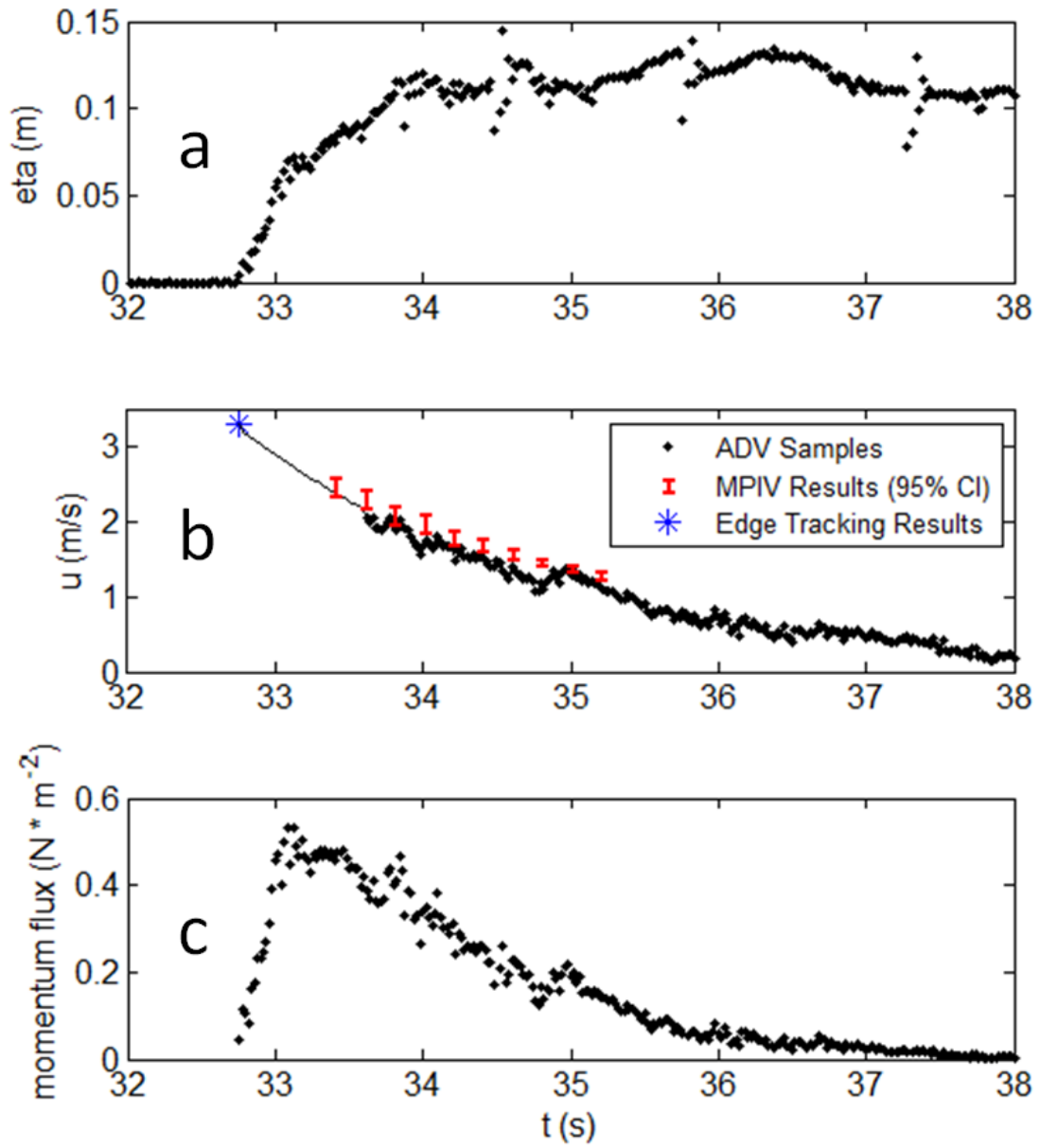
**Figure 6:** Breakdown of momentum flux for 'Kinematics' Trial 15 at X = 31.89 m, Y = 0.54 m for ERF=7s wave. (a) Wave height as measured by USWG4. (b) Fluid velocity measurements from leading edge tracking (blue star), MPIV analysis (red error bars, 95% confidence interval), and ADV2 (black dots). Best-fit line (black) used to calculate momentum flux. (c) Momentum flux.
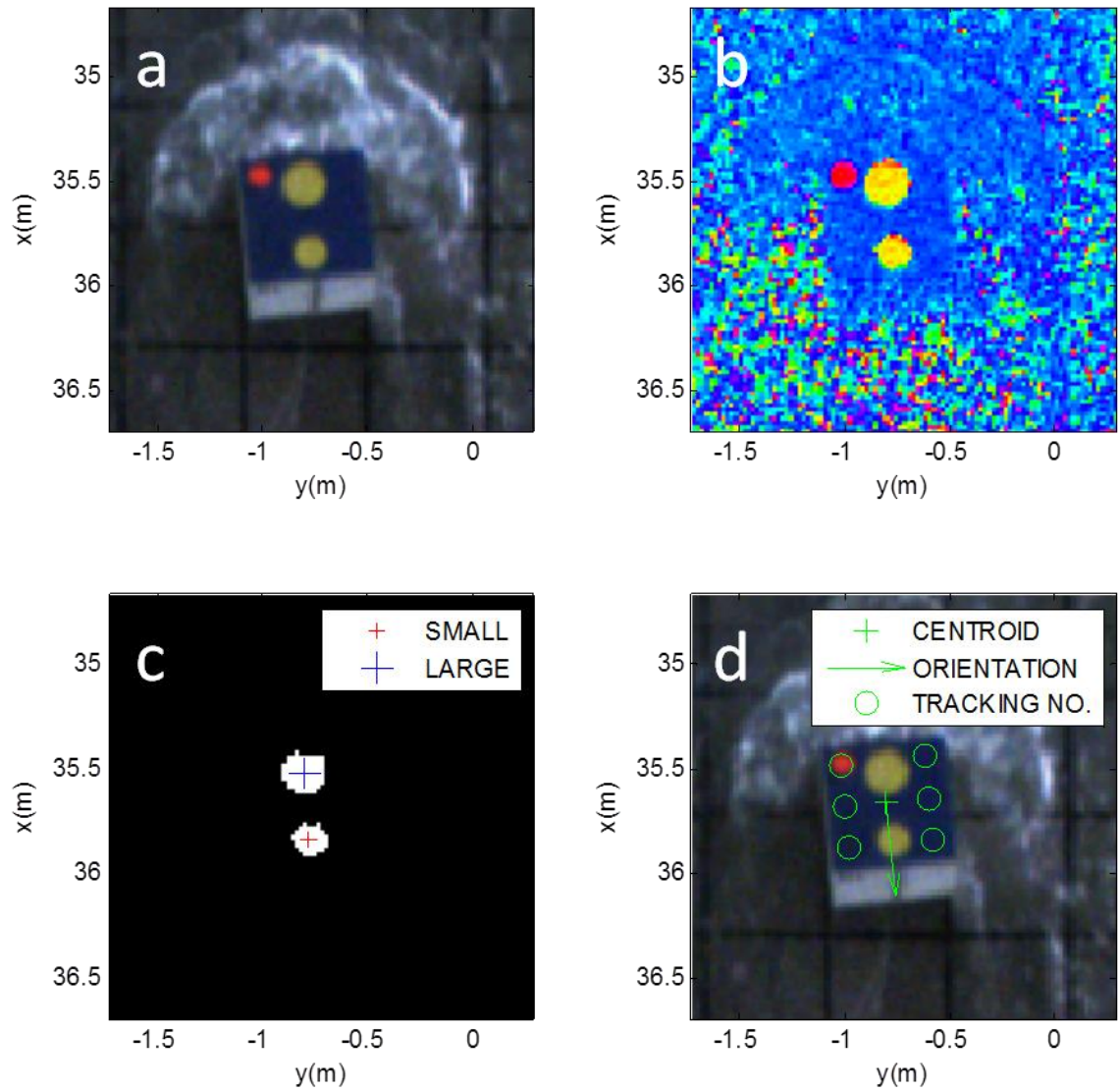
**Figure 7:** Four steps of the box tracking process. (a) Original image rectified to box lid height. (b) "Hue" channel isolated using HSV color map. (c) Yellow dots located and identified by size. (d) Tracking results plotted over original image.
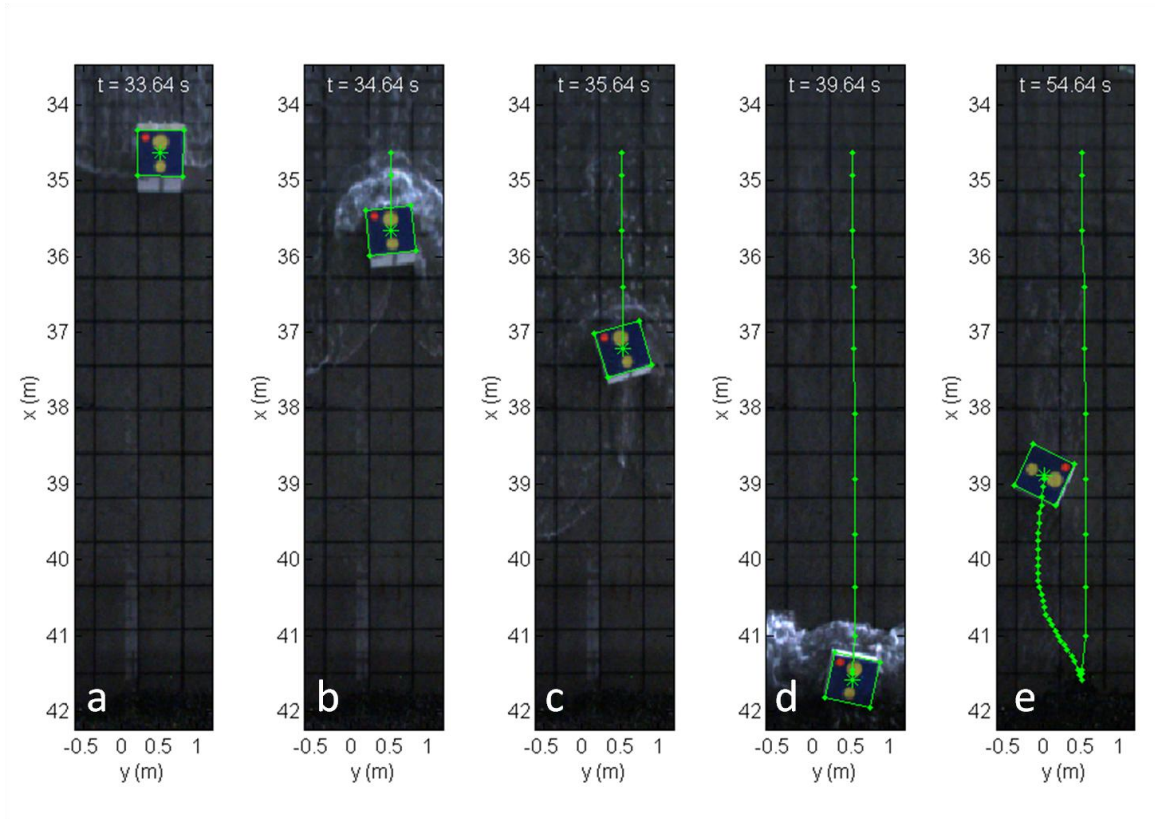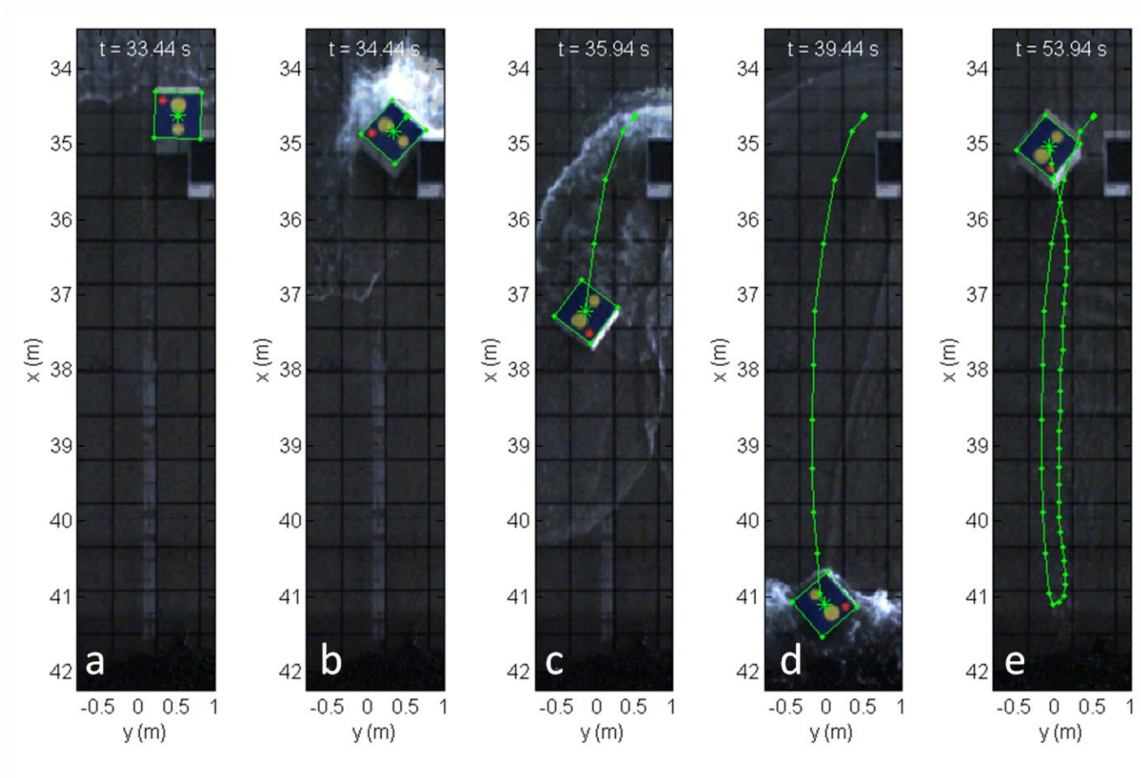
**Figure 8:** Cropped, merged images from Trial 30. Boxes arranged in Config 1. Each image (a-e) is from a specific frame with time indicated at top of image. Box tracking algorithm is demonstrated by box outline (green) and box center position (green star). Box velocity can be inferred from green dot spacing; frame rate is 2 Hz.
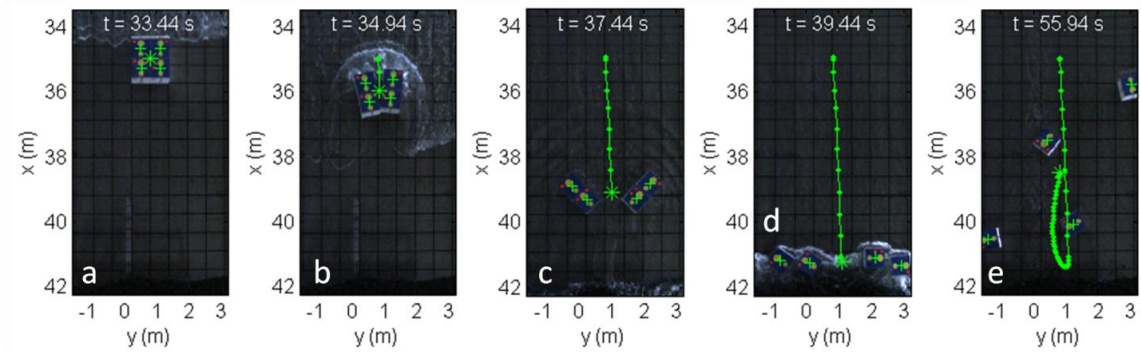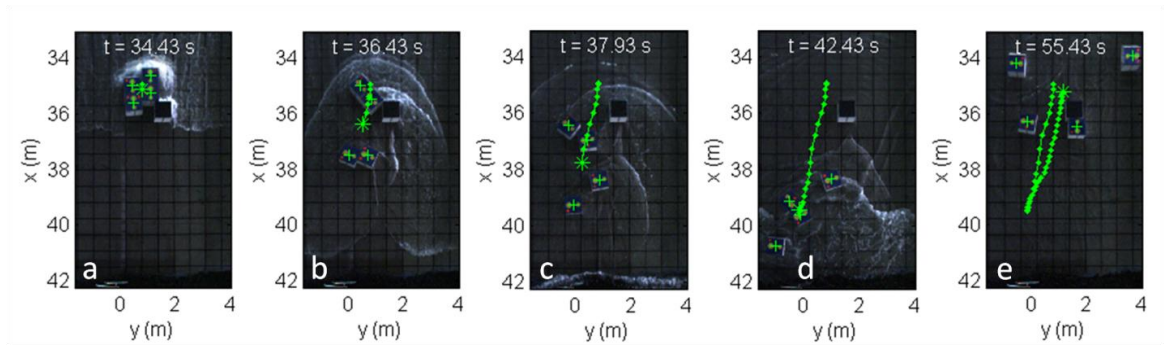
**Figure 9:** Cropped, merged images from Trial 31. Boxes arranged in Config 2. Each image (a-e) is from a specific frame with time indicated at top of image. Box tracking algorithm is demonstrated by box outline (green) and box center position (green star). Box velocity can be inferred from green dot spacing; frame rate is 2 Hz.

**Figure 10:** Cropped, merged images from Trial 32. Boxes arranged in Config 3. Each image (a-e) is from a specific frame with time indicated at top of image. Box tracking algorithm is demonstrated by box centers (green crosses). Centroid (green star) is the arithmetic mean of all box centers. Centroid velocity can be inferred from green dot spacing; frame rate is 2 Hz.
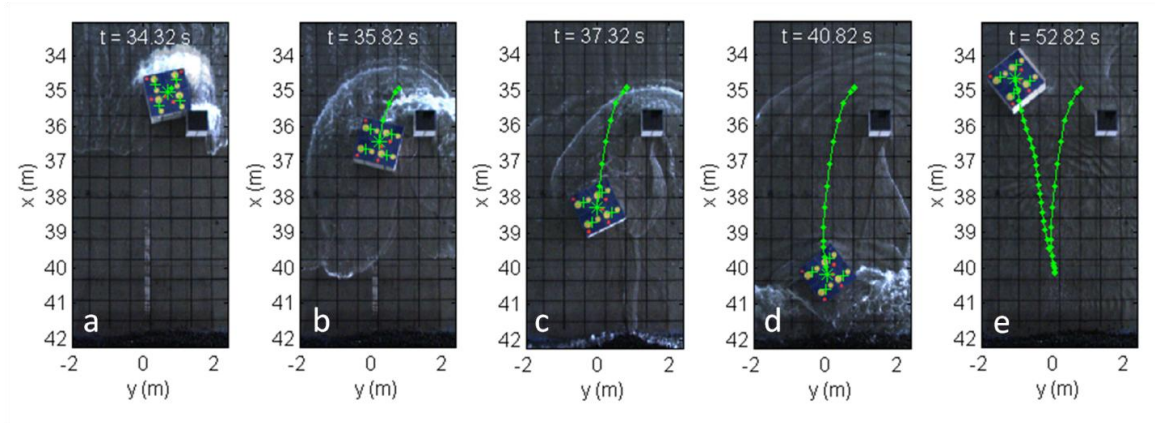
**Figure 11:** Cropped, merged images from Trial 33. Boxes arranged in Config 4. Each image (a-e) is from a specific frame with time indicated at top of image. Box tracking algorithm is demonstrated by box centers (green crosses). Centroid (green star) is the arithmetic mean of all box centers. Centroid velocity can be inferred from green dot spacing; frame rate is 2 Hz.
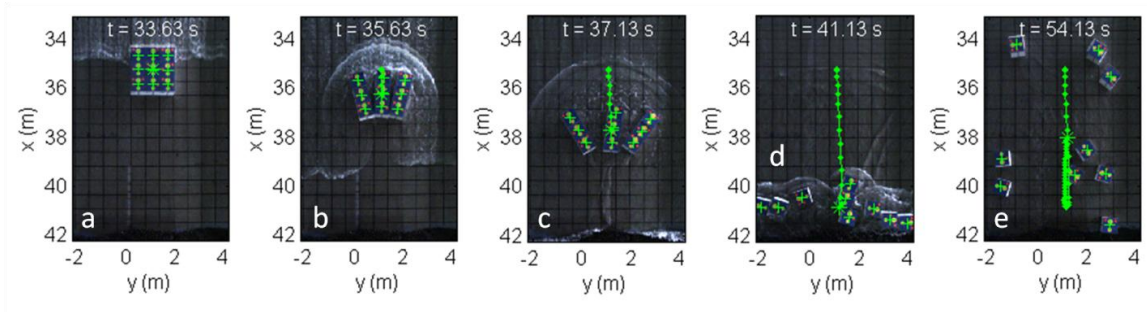
**Figure 12:** Cropped, merged images from Trial 65. Boxes arranged in Config 12. Each image (a-e) is from a specific frame with time indicated at top of image. Box tracking algorithm is demonstrated by box centers (green crosses). Centroid (green star) is the arithmetic mean of all box centers. Centroid velocity can be inferred from green dot spacing; frame rate is 2 Hz.
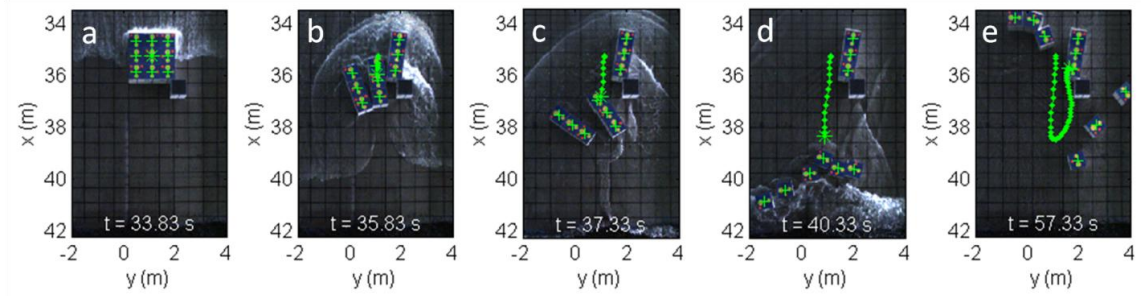
**Figure 13:** Cropped, merged images from Trial 36. Boxes arranged in Config 7. Each image (a-e) is from a specific frame with time indicated at top of image. Box tracking algorithm is demonstrated by box centers (green crosses). Centroid (green star) is the arithmetic mean of all box centers. Centroid velocity can be inferred from green dot spacing; frame rate is 2 Hz.

**Figure 14:** Cropped, merged images from Trial 37. Boxes arranged in Config 8. Each image (a-e) is from a specific frame with time indicated at top of image. Box tracking algorithm is demonstrated by box centers (green crosses). Centroid (green star) is the arithmetic mean of all box centers. Centroid velocity can be inferred from green dot spacing; frame rate is 2 Hz.
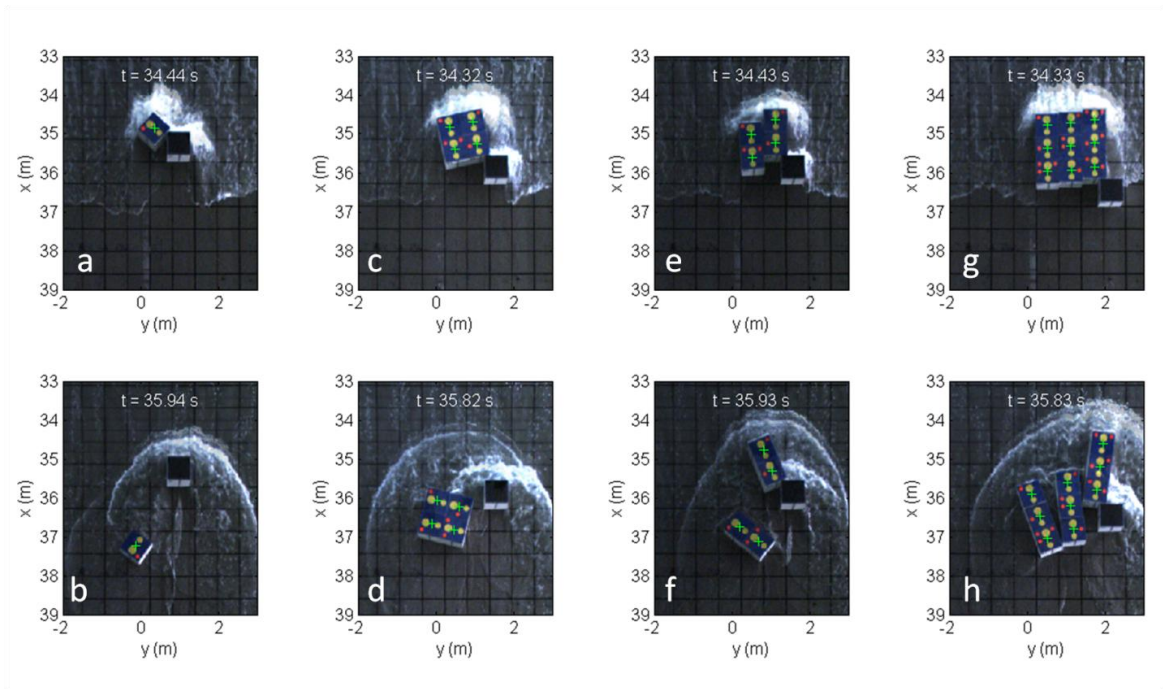
**Figure 15:** Comparison of cropped, merged images at similar times across four trial, chosen as follows: (a-b) Trial 31, Config 2; (c-d) Trial 65, Config 12; (e-f) Trial 33, Config 4; (g-h) Trial 37, Config 8. Each image (a-h) is from a specific frame with time indicated at top of image. Box tracking algorithm is demonstrated by box centers (green crosses).
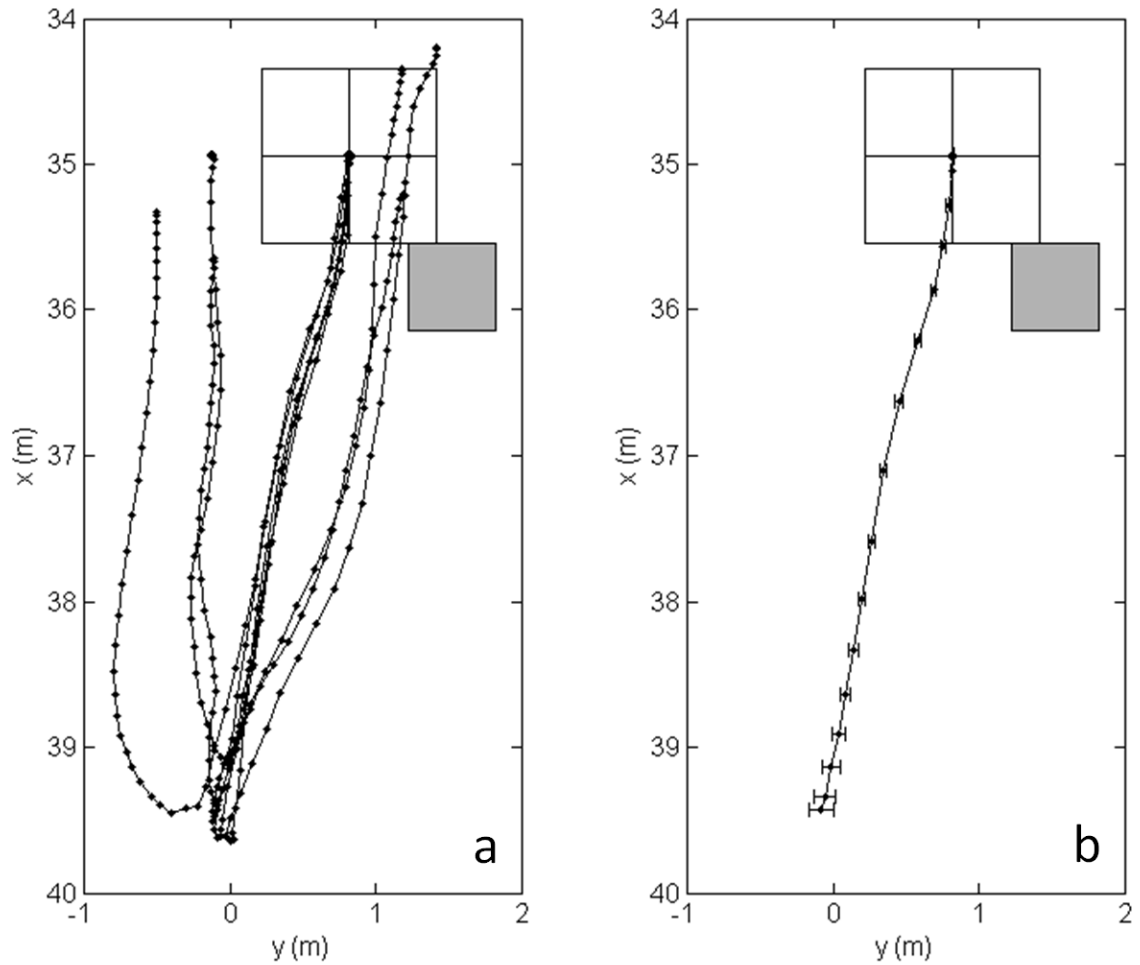
**Figure 16:** Repeatability of centroid path for Config 4 over six trials (Trial 33, 39-43). For each trial, (a) shows the box centroid positions (black dots); the centroid is the arithmetic mean of all box centers for a single time step. (b) shows the mean centroid path across all six trials for the onshore (+X-direction) motion only. Error bars in (b) show standard error of Y-position at each time step with 95% confidence interval. Schematic of initial box positions from Table 1 shown for Config 4 in both plots for reference and scale.
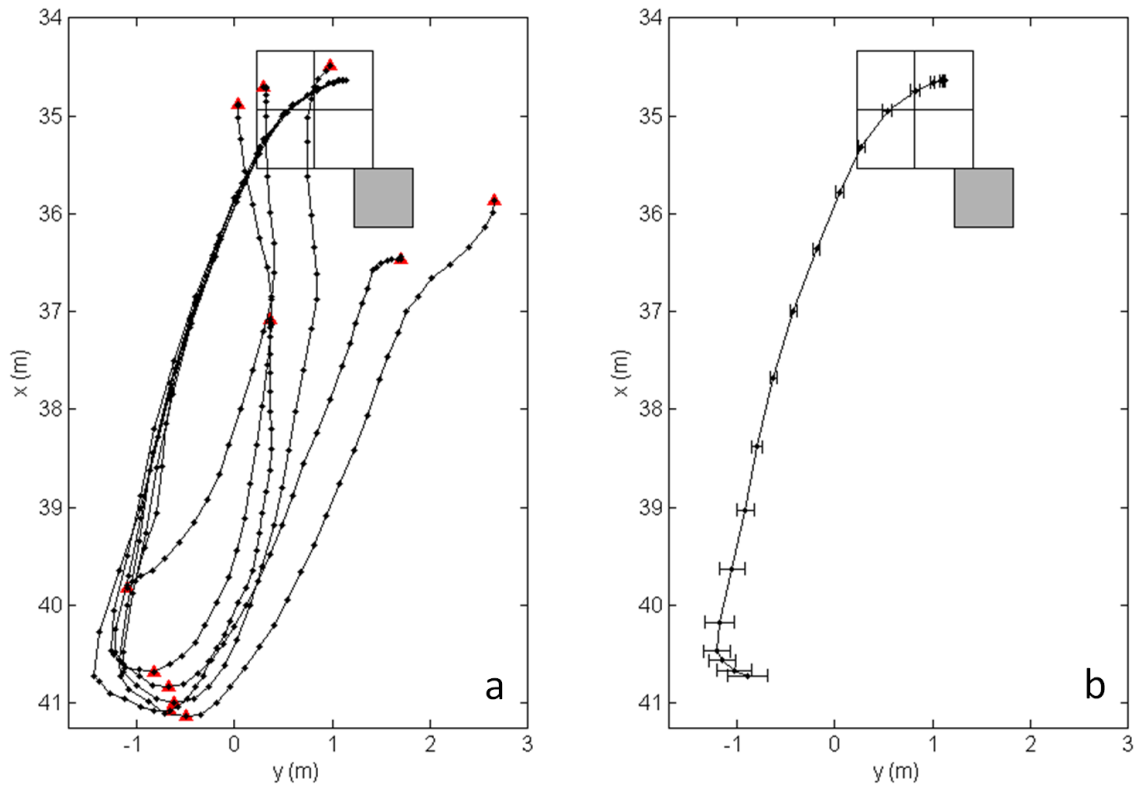
**Figure 17:** Repeatability of Box 2 path for Config 4 over six trials (Trial 33, 39-43). For each trial, (a) shows the Box 2 center positions (black dots), "stall points" where X-velocity reverses (red triangles), and "stop points" where the box settles (red triangles). (b) shows the mean Box 2 path across all six trials for the onshore (+X-direction) motion only. Error bars in (b) show standard error of Y-position at each time step with 95% confidence interval. Schematic of initial box positions from Table 1 shown for Config 4 in both plots for reference and scale.
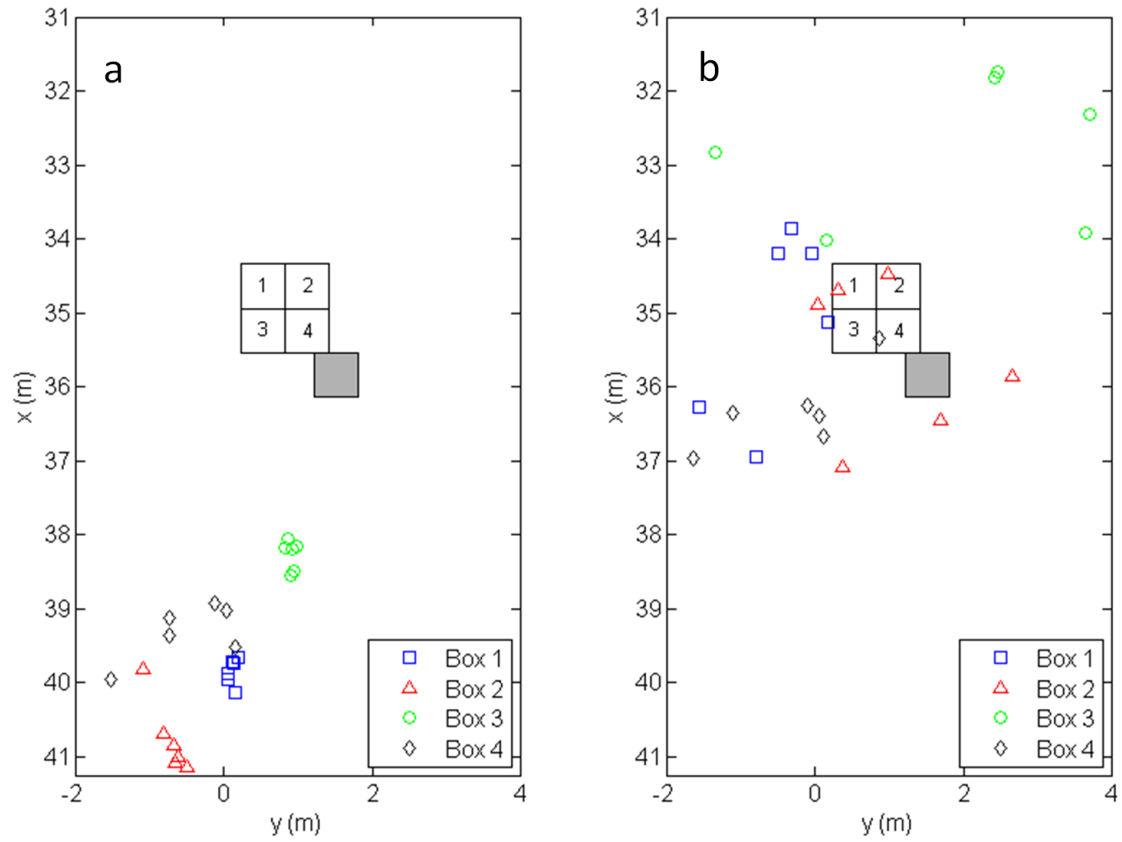
**Figure 18:** Repeatability of Config 4 expressed via stall points and stop points for each box over six trials (Trial 33, 39-43). Stall points (a) are the positions where cross-shore (X) velocity reverses from onshore (+X) to offshore (-X) due to the reflected wave. Stop points (b) are the final positions of each box at the end of the trial. Schematic of initial box positions from Table 1 shown for Config 4 in both plots for reference and scale. Box numbers in schematic correspond to symbols specified in legend.
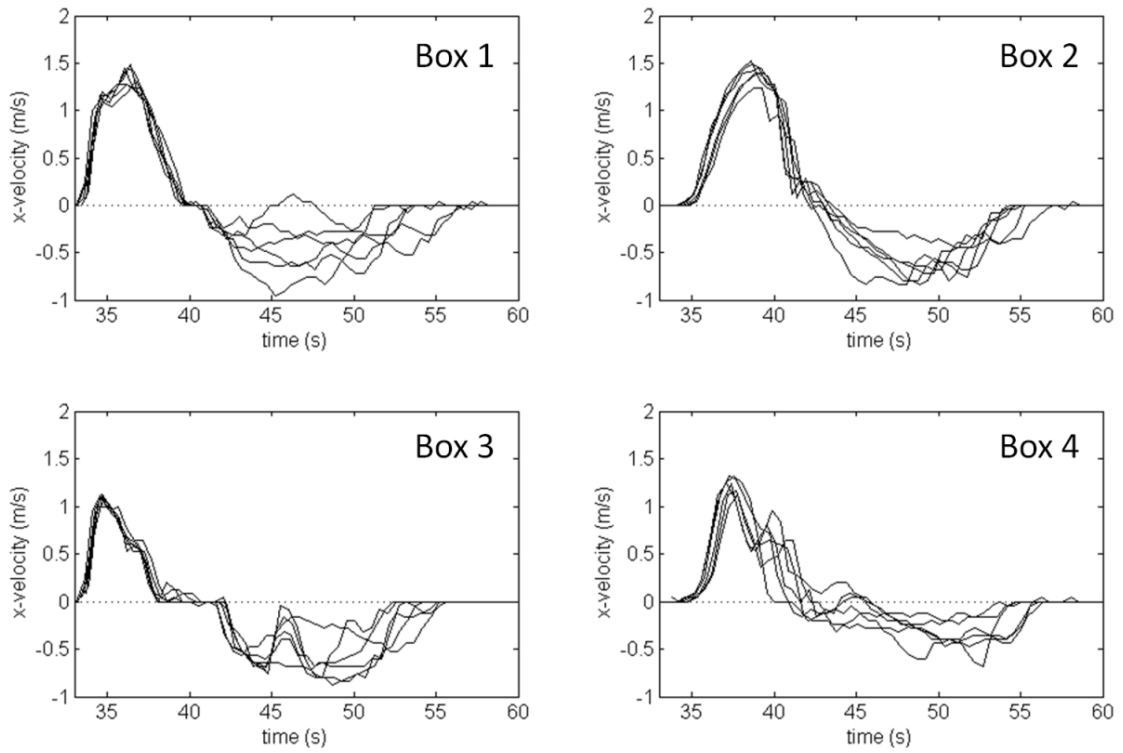
**Figure 19:** Velocity repeatability for six trials (Trial 33, 39-43) conducted with Config 4. Each plot shows cross-shore (X) velocity for a single box co-plotted over time for all six trials. See schematic in Figure 18 for box numbering.
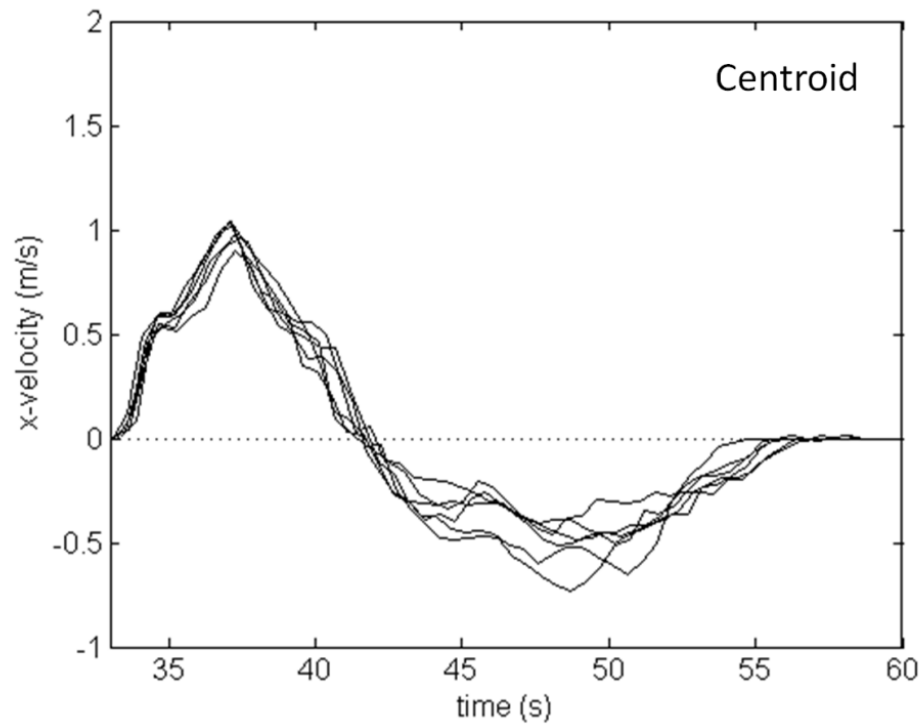
**Figure 20:** Centroid velocity repeatability for six trials (Trial 33, 39-43) conducted with Config 4. Plot shows cross-shore (X) velocity for centroid of all four boxes co-plotted over time for all six trials. The centroid is the arithmetic mean of all box centers for a single time step.
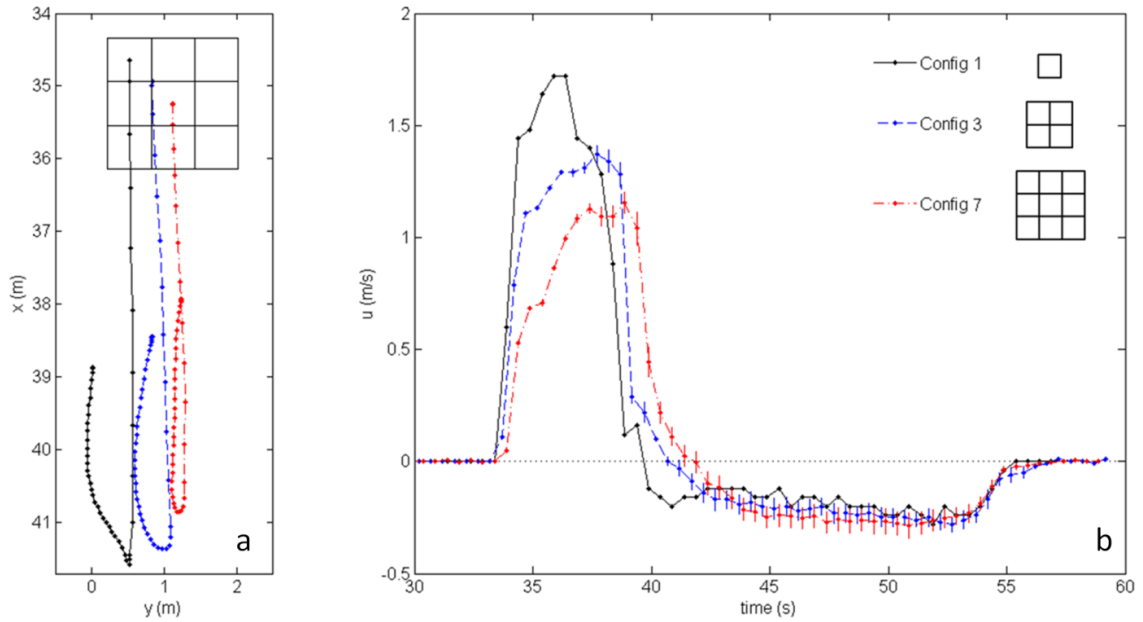
**Figure 21:** Centroid paths (a) and cross-shore (X-direction) centroid velocity (b) for Configs 1, 3, and 7. Positions (a) and velocities (b) for multi-box configurations (Configs 3 and 7) are for the centroid, which is the arithmetic mean of all box centers for a single time step. Error bars for multi-box configurations represent standard error of box velocities with 95% confidence intervals. Schematic of initial box positions from Table 1 shown for Config 7 in plot (a) for reference and scale.

**Figure 22:** Centroid paths (a) and cross-shore (X-direction) centroid velocity (b) for Configs 2, 4, and 8. Positions (a) and velocities (b) for Configs 4 and 8 are for the centroid of all sliding boxes. Schematic of initial box positions from Table 1 shown for Config 8 in plot (a) for reference and scale.
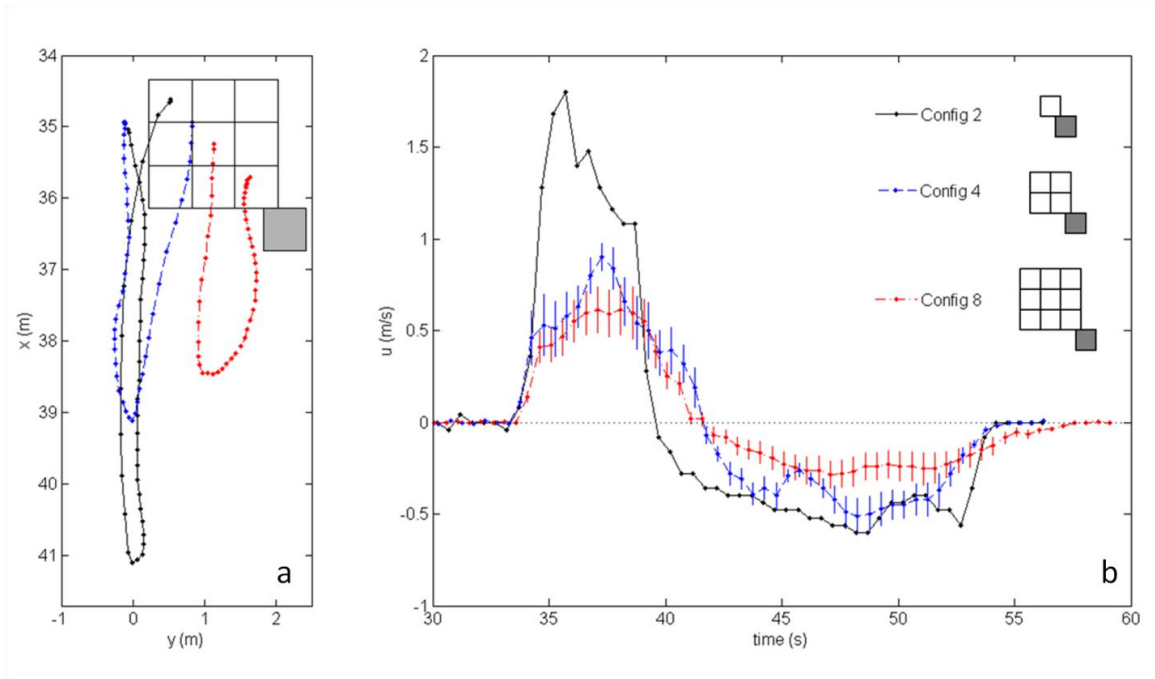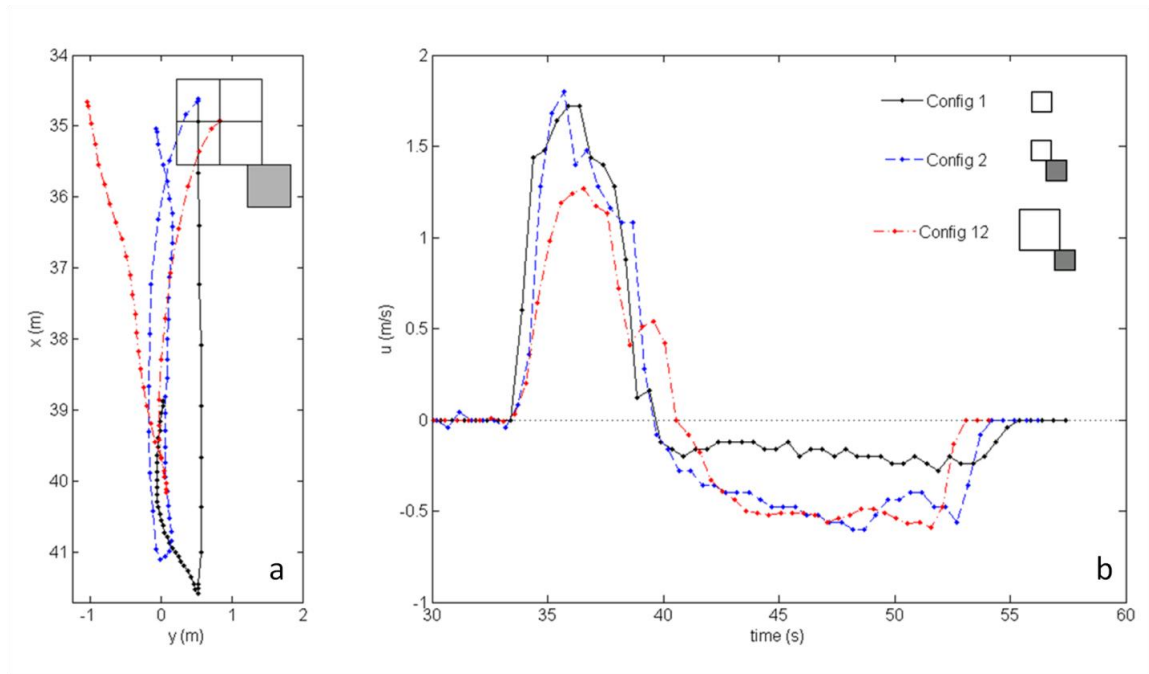
**Figure 23:** Centroid paths (a) and cross-shore (X-direction) centroid velocity (b) for Configs 1, 2, and 12. Positions (a) and velocities (b) for Config 12 are for the center of the four-box square. Schematic of initial box positions from Table 1 shown for Config 12 in plot (a) for reference and scale.
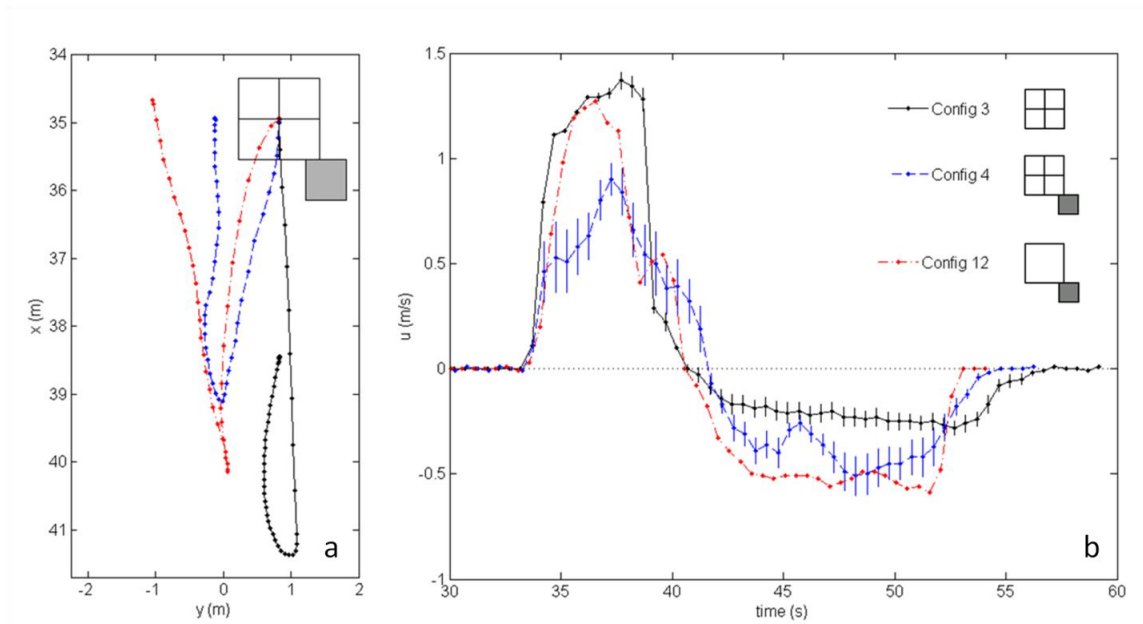
**Figure 24:** Centroid paths (a) and cross-shore (X-direction) centroid velocity (b) for Configs 3, 4, and 12. Only Trial 33 is used to represent Config 4. Positions (a) and velocities (b) for multi-box configurations (Configs 3 and 4) are for the centroid, which is the arithmetic mean of all box centers for a single time step. Positions (a) and velocities (b) for Config 12 are for the center of the four-box square. Error bars for multi-box configurations represent standard error of box velocities with 95% confidence intervals. Schematic of initial box positions from Table 1 shown for Config 4 in plot (a) for reference and scale.

## Bibliography

Arikawa, T. and Yashizaki, M. (2009) "Large Scale Tests on Concrete Wall Destruction by Tsunami with Driftwood," *Proc. Conference on Coastal Engineering*, Japan Society of Civil Engineering, (in Japanese).

Arikawa, T., Ohtsubo, D., Nakano, F., Shimosako, K., Ishikawa, N. (2009) "Large Model Tests of Drifting Container Impact Force due to Surge Front Tsunami," *Proc. Conference on Coastal Engineering*, Japan Society of Civil Engineering, (in Japanese).

Baldock, T.E., Cox, D. Maddux, T., Killian, J., Fayler, L. (2009) "Kinematics of breaking tsunami wavefronts: A data set from large scale laboratory experiments," *Coastal Engineering*, 56, 506-516.

Bridges K., Cox, D., Thomas, S., Shin, S., and Rueben, M. (2010) "Influence of macro-roughness on tsunami runup and forces: Large scale experiments at the NEES Tsunami Facility," *Coastal Engineering*, Submitted 12/2010.

Cox, D., Tomita, T., Lynett, P., and Holman, R. A. (2008). "Tsunami inundation with macro-roughness in the constructed environment." *Proc. 31st Int. Conf. on Coastal Engineering*, ASCE, New York, 1421–1432.

Goring, D.G. (1978). "Tsunamis – the propagation of long waves onto a shelf," REP Kh-R-38, W.M. Keck Lab. of Hyd. and Water Resources, Calif. Inst. Technology., California.

Grilli, S. T., Ioualalen, M., Asavanant, J., Shi, F., Kirby, J. T., Watts, P., (2007) Source constraints and model simulation of the December 26, 2004, Indian Ocean Tsunami, *Journal of Waterway, Port, Coastal and Ocean Engineering*, Special Issue on Tsunami Engineering, 133, 6, 414-428.

Groat, C. G. (2005). "Statement of C. G. Groat, Director, U.S. Geological Survey, U.S. Dept. of the Interior." Statement before the Committee of Science, January 26, U.S. House of Representatives, Washington, DC.

Holman, R. A., and J. Stanley (2007) "The history and technical capabilities of Argus," *Coastal Engineering*, 54, 477-491.

Liu, P.L.-F., Cho, Y.-S., Briggs, M.J., Kanoglu, U. and Synolakis, C.E. (1995). "Runup of solitary waves on a circular island." *J. of Fluid Mechanics*, 302, 259-285.

Lynett, P., Wu, T.-R., and Liu, P. L.-F. (2002). "Modeling Wave Runup with Depth-Integrated Equations," *Coastal Engineering*, v. 46(2), p. 89-107.

Lynett, P.J. (2007) Effect of a Shallow Water Obstruction on Long Wave Runup and Overland Flow Velocity," *J. of Waterway, Port, Coastal and Ocean Engineering*, 133, 6, 455-462.

Madsen, P. A., Fuhrman, D.R., Schaffer, H.A. (2008) "On the solitary wave paradigm for tsunamis," *J. Geophysical Research*, Vol 113, C12012.

Matsutomi, H. (2009). "Method for Estimating Collision Force of Driftwood Accompanying Tsunami Inundation Flow." *Journal of Disaster Research,* Vol. 4, No. 6, 435-440.

Mori, N., T. Takahashi, T. Yasuda, and H. Yanagisawa (2011). "Survey of 2011 Tohoku earthquake tsunami inundation and run-up." *Geophys. Res. Lett.*, 38, L00G14.

Okal, Emile A., Fritz, Hermann M., Synolakis, Costas E., Borrero, Jose C., Weiss, Robert, Lynett, Patrick J., Titov, Vasily V., Foteinis, Spyros, Jaffe, Bruce E., Liu, Philip L.-F., and Chan, I-chi (2010). "Field Survey of the Samoa Tsunami of 29 September 2009." *Seismological Research Letters*, Vol. 81, No. 4, July/August 2010, 577-591.

Oshnack, M.B., Aguiniga, F., Cox, D., Gupta, R., van de Lindt, J. (2009). "Effectiveness of Small Onshore Seawalls in Reducing Forces Induced by Tsunami Bore: Large Scale Experimental Study." *Journal of Disaster Research*, Vol.4 No.6, 382-390.

Oshnack, M.B., Shin, S., Cox, D., Galan, F., Knight, A. (2010). "Cross-Shore Variation of Tsunami Loads on Vertical Walls: Transition from Impulse Loads to Quasi-Steady Bores." *Journal of Waterway, Port, and Coastal Engineering,* (in review).

Park, S., van de Lindt, J.W., Cox, D., Gupta, R., Aguiniga, F. (2010). "Methodology for Development of Tsunami Fragilities," ASCE, *Journal of Structural Engineering*, (in review).

Pomonis et al. (2006). "The Indian Ocean Tsunami of 26 December 2004: Mission Findings in Sri Lanka and Thailand." United Kingdom: Institution of Structural Engineers.

Riggs, H.R., Robertson, I.N., Cheung, K.F., Pawlak, G., Young, Y.L., Yim, S.C.S. (2008). "Experimental simulation of tsunami hazards to buildings and bridges," *Proc., NSF CMMI Engineering Research and Innovation Conference*, Paper No. 0530759.

Roeber, V., Cheung, K.F., and Kobayashi, M.H. (2010). Shock-capturing Boussinesq-type model for nearshore wave processes, *Coastal Engineering*, 57, 407-423.

Ruangrassamee, A., Yanagisawa, H., Foytong, P., Lukkunaprasit, P., Koshimura, S., and Imamura, F. (2006). "Investigation of tsunami-induced damage and fragility of buildings in Thailand after the December 2004 Indian Ocean tsunami." *Earthquake Spectra*, 22(S3), S377–S401.

Saatcioglu et al. (2006). "Performance of Structures in Thailand During the December 2004 Great Sumatra Earthquake and Indian Ocean Tsunami." *Earthquake Spectra*, 22, S355-S375.

Swigler, D. and Lynett, P. (2010). "Laboratory Study of the Three-Dimensional Turbulence and Kinematic Properties Associated with a Solitary Wave Traveling Over an Alongshore-Variable, Shallow Shelf." in review.

Takahashi, S., Sugano, T., Tomita, T., Arikawa, T., Tatsumi, D., Kashima, H., Murata, S., Matsuoka, Y., Nakamura, T. (2010). "Summary Report on Joint Survey for 2010 Chilean Earthquake and Tsunami Disaster in Ports and Coasts." *Technical Report of the Port and Airport Research Institute*, Kuriyama, Japan.

Thomas, S. and Cox, D. (2010) "Influence of Finite-Length Seawalls for Tsunami Loading on Coastal Structures," *Journal of Waterway, Port, and Coastal Engineering*, 138, 203-214.

Titov, V.V. and Synolakis, C.E. (1995) "Modeling of Breaking and Nonbreaking Long Wave Evolution and Runup using VTCS-2," *J. of Waterway, Port, Coastal and Ocean Engineering*., 121, 6, 308-316.

Tomita, T., Honda, K., Kakinuma, T. (2006) "Application of three-dimensional tsunami simulator to estimation of tsunami behavior around structures, *Proc. Int. Conf. on Coastal Engineering*, San Diego., Vol 2, 1677 – 1688.

Tomita, T. and Honda, K. (2009) "Tsunami estimation including effect of coastal structures and buildings by 3D model" *Proc. Coastal Structures '07*, Am. Soc. Civil Engineers, Vol 1, 681 – 692.

USGS Tsunami Pilot Study Working Group. (2006). "Seaside, Oregon tsunami pilot study—Modernization of FEMA flood hazard maps." *Open-File Rep. 2006-1234*, U.S. Dept. of the Interior, U.S. Geological Survey, Washington, DC.

van de Lindt, J.W., Gupta, R., Garcia, R., and Wilson, J. (2008). "Tsunami bore forces on a compliant residential building model," *Engineering Structures,* (in press).

Yeom, G., Nakamura, T., and Mizutani, N. (2009). "Collision Analysis of Container Drifted by Runup Tsunami Using Drift Collision Model." *Journal of Disaster Research,* Vol 4. No. 6, 441-449.